EUROPEAN ORGANIZATION FOR NUCLEAR RESEARCH

CERN-EP/99–001
6. January 1999

The NA49 Large Acceptance Hadron Detector

S. Afanasiev[9], T. Alber[13], H. Appelshäuser[7,#], J. Bächler[5], D. Barna[4], L.S. Barnby[3], J. Bartke[6], R.A. Barton[3], L. Betev[11], H. Bialkowska[14,5], F. Bieser[2], A. Billmeier[10], C.O. Blyth[3], R. Bock[7], C. Bormann[10], J. Bracinik[19], F.P. Brady[8], R. Brockmann[7,†], R. Brun[5], P. Buncic[5,10], H.L. Caines[3], D. Cebra[8], G.E. Cooper[2], J.G. Cramer[16], P. Csato[4], M. Cyprian[12], J. Dunn[8], V. Eckardt[13], F. Eckhardt[12], T. Empl[20], J. Eschke[7], M.I. Ferguson[11], H. Fessler[13], H.G. Fischer[5], D. Flierl[10], Z. Fodor[4], U. Frankenfeld[7], P. Foka[10,*], P. Freund[13], V. Friese[12], J. Ftacnik[19], M. Fuchs[10], F. Gabler[10], J. Gal[4], R. Ganz[13], M. Gaździcki[10], E. Gładysz[6], J. Grebieszkow[15], J. Günther[10], J.W. Harris[17], S. Hegyi[4], T. Henkel[12], L.A. Hill[3], V. Hlinka[19], I. Huang[2,8], H. Hümmler[10,13], G. Igo[11], D. Irmscher[2,7], M. Ivanov[19], R. Janik[19], P. Jacobs[2], P.G. Jones[3], K. Kadija[18,13], V.I. Kolesnikov[9], M. Kowalski[6], B. Lasiuk[17], P. Lévai[4], K. Liebicher[13], U. Lynen[7], A.I. Malakhov[9], S. Margetis[2,$], C. Markert[7], C. Marks[2], B. Mayes[20],G.L. Melkumov[9], A. Mock[13], J. Molnár[4], J.M. Nelson[3], M. Oldenburg[10], G. Odyniec[2], G. Palla[4], A.D. Panagiotou[1], Y. Pestov[7], A. Petridis[1], M. Pikna[19], W. Pimpl[13], L. Pinsky[20], A. Piper[12], R.J. Porter[2], A.M. Poskanzer[2], S. Poziombka[10], D.J. Prindle[16], F. Pühlhofer[12], W. Rauch[13], J.G. Reid[16], R. Renfordt[10], W. Retyk[15], H.G. Ritter[2], D. Röhrich[10], C. Roland[7], G. Roland[10], H. Rudolph[2,10], A. Rybicki[6], T. Sammer[13], A. Sandoval[7], H. Sann[7], E. Schäfer[13], R. Schmidt[7], D. Schmischke[10], N. Schmitz[13], S. Schönfelder[13], A.Yu. Semenov[9], J. Seyboth[13], P. Seyboth[13], J. Seyerlein[13], F. Sikler[4,5], B. Sitar[19], E. Skrzypczak[15], G.T.A. Squier[3], H. Stelzer[7], R. Stock[10],P. Strmen[19], H. Ströbele[10], C. Struck[12], T. Susa[18], I. Szarka[19], I. Szentpetery[4], P. Szymański[5,14], J. Sziklai[4], M. Toy[2,11], T.A. Trainor[16], S. Trentalange[11], T. Ullrich[17], M. Vassiliou[1], G. Veres[4], G. Vesztergombi[4], D. Vranic[5,18], F.Q. Wang[2], D.D. Weerasundara[16], S. Wenig[5], C. Whitten[11], H. Wieman[2], T. Wienold[2,#], L. Wood[8], T.A. Yates[3], J. Zimanyi[4], X.-Z. Zhu[16], R. Zybert[3]

[1]Department of Physics, University of Athens, Athens, Greece, [2]Lawrence Berkeley National Laboratory, University of California, Berkeley, USA, [3]Birmingham University, Birmingham, England, [4]KFKI Research Institute for Particle and Nuclear Physics, Budapest, Hungary, [5]CERN, Geneva, Switzerland, [6]Institute of Nuclear Physics, Cracow, Poland, [7]Gesellschaft für Schwerionenforschung (GSI), Darmstadt, Germany, [8]University of California at Davis, Davis, USA, [9]Joint Institute for Nuclear Research, Dubna, Russia, [10]Fachbereich Physik der Universität, Frankfurt, Germany, [11]University of California at Los Angeles, Los Angeles, USA, [12]Fachbereich Physik der Universität, Marburg, Germany, [13]Max-Planck-Institut für Physik, Munich, Germany, [14]Institute for Nuclear Studies, Warsaw, Poland, [15]Institute for Experimental Physics, University of Warsaw, Warsaw, Poland, [16]Nuclear Physics Laboratory, University of Washington, Seattle, WA, USA, [17]Yale University, New Haven, CT, USA, [18]Rudjer Boskovic Institute, Zagreb, Croatia, [19]Comenius University, Bratislava, Slovakia, [20]University of Houston, Houston, TX, USA

[†]deceased [*]EC-fellow [#]now: Physikalisches Institut, Universität Heidelberg, Germany [$]now: Kent State Univ., Kent, OH, USA

Table of Contents

Abstract

The NA49 detector is a wide acceptance spectrometer for the study of hadron production in p+p, p+A, and A+A collisions at the CERN SPS. The main components are 4 large volume TPCs for tracking and particle identification via dE/dx. TOF scintillator arrays complement particle identification. Calorimeters for transverse energy determination and triggering, a detector for centrality selection in p+A collisions, and beam definition detectors complete the set-up.

A description of all detector components is given with emphasis on new technical realizations. Performance and operational experience are discussed in particular with respect to the high track density environment of central Pb+Pb collisions.

Submitted to Nucl. Instr. Meth. A

1 Introduction

The physics of hadronic interactions can today be studied using many different initial conditions. These range from the most elementary hadron+nucleon systems, via a multitude of possible hadron+nucleus combinations, up to the realm of heavy ion collisions. In this last field the recent acceleration of Pb–ion beams at the CERN SPS has provided the largest, most energy-dense collision system of hadrons so far available for controlled inspection in the laboratory.

The NA49 experiment was conceived to cope with these most complex initial conditions, as it is generally expected that in the region of extreme energy densities the transition to a new state of hadronic matter, the quark-gluon plasma, might occur.

The corresponding spectrum of hadronic final states exhibits an extremely rich phenomenology. The multiplicity of produced charged hadrons, to quote one example, may vary from typically 10 in nucleon+nucleon interactions to more than 10^3 per event in central Pb+Pb collisions.

The experimental study of this phenomenology presents a very considerable challenge. On one hand, this has to do with the fact that there is no reliable theoretical basis for the description of soft hadronic processes in the non-perturbative sector of Quantum Chromodynamics. On the other hand, and as a consequence, any attempt at detailed experimental understanding has to rely on self-consistent, complete data sets which fully exploit the internal structure of these interactions. Large solid angle detectors for particle tracking and momentum determination as well as particle identification over a major fraction of phase space are therefore mandatory. At the CERN SPS, with its fixed target kinematics and particle beams in the momentum range of 100–200 GeV/c per nucleon, this aim can be met with state-of-the-art detector technology.

The NA49 detector has been designed, with these necessities in mind, to be able to handle the most complex hadronic final states and to search for tangible signatures of the elusive quark-gluon plasma state.

It consists of a wide acceptance magnetic spectrometer combining momentum measurement and particle identification in a set of large Time Projection Chambers, backed up with additional particle identifiers and calorimeters. It aims at covering, with the same set-up, the complete range of hadronic interactions described above, up to the highest particle densities produced in central Pb+Pb collisions.

2 Detector Concept

The NA49 detector concept is based on the following design considerations:

- The experiment is conceived around two existing, superconducting dipole magnets [1], offering a total bending power of up to 9 Tm over 7 m length. The magnets determine –by their available magnetic field volume and by their downstream aperture– to a large extent the phase space available for tracking.
- The extreme particle multiplicities and densities encountered in heavy ion collisions necessitate unprecedented multi-particle pattern recognition and separation capabilities. In addition, the large base length of the experiment calls for separated, large volume track detectors with a minimum of material in the acceptance in order to minimize the rate of secondary interactions and multiple scattering.
- The aim at large solid angle particle identification suggests a combination of tracking and identification in the track detectors.
- The data acquisition capability of the detector should allow for the accumulation of about 20 events per burst for the highest multiplicity heavy ion events in order to reach a desired total event number of 10^6 per beam period at the CERN SPS accelerator.

The constraints and requirements mentioned above can be met by Time Projection Chambers (TPC) with their superior pattern recognition and energy loss measurement capabilities, adequate two-particle and space resolution, and their large, "empty" gas volumes. It has been shown [2],[3] that this detector type can work in very high track density environment with pad readout only, providing the same resolution in energy loss measurement as conventional wire readout.

The NA49 tracking system is therefore built up by four large volume TPCs. This system is completely stand-alone, without additional external coordinate determination except for the incoming beam particle.

It should also be mentioned that the TPC concept limits –by way of the considerable open time of the detectors– the range of possible beam intensities to less than about 10^5 per second. For the use of a typical 1% interaction length target this means that the data acquisition rate can be saturated with a modest trigger reduction of order 10^2. In view of the inherent difficulty of obtaining a fast trigger decision from the TPC itself this has to be achieved by additional trigger detectors.

Further design considerations follow from this basic detector choice:

- The TPC system deploys two "Vertex" chambers (VTPC-1/2) inside the magnets and two "Main" chambers (MTPC-L/R) on both sides of the beam behind the magnets (see Fig. 1). The latter chambers have a length of 4 m in order to meet the requirements of dE/dx resolution in the relativistic rise.
- Energy loss measurements have to be backed up by independent methods in the region of minimum ionization, $\beta\gamma \simeq 3$. Four walls of Time-of-Flight (TOF) scintillator detectors are therefore installed behind the MTPCs. In order to extend TOF determination into backward cms rapidity arrays of PesTOF counters are positioned in a plane between the two magnets.
- Although it is in principle possible to channel a proton beam of the above mentioned intensity through the active area of a gated TPC, this is excluded for a Pb–beam with almost 10^4 times higher ionization density. As it seemed technically not feasible to install a vacuum chamber in the drift field without jeopardizing the required track reconstruction performance and detector gas quality, a solution with split field cage and low density detector gas was chosen for the VTPCs where the beam runs through the full length of each detector between two identical drift cages. This ensures at the same time the necessary cutoff of the extremely high track densities in the neighbourhood of the beam. In this concept, the walls of the TPC gas envelope and drift cage have to be thin, i.e. comparable to the radiation length of the detector gas. Helium bags in front and behind the VTPCs and in between the MTPCs further reduce δ-electron production due to beam particles.
- Two downstream calorimeters complete the particle detection coverage and serve as trigger devices in heavy ion running.
- A versatile set of target stations including a liquid hydrogen target, combined with a set of trigger counters is used for the different running conditions and event definition with hadron and ion beams.
- A special target detector measures the number of target recoil ("grey") protons from nuclear targets. This allows determination of and triggering on impact parameter in p+nucleus collisions.

The resulting detector layout is shown in Fig. 1. The acceptance coverage of the tracking system amounts to about 80% of all charged particles produced in hadronic interactions at 158 GeV/c beam momentum. The acceptance losses are concentrated in the backward region

below –1 unit of cms rapidity, in the extreme forward region at longitudinal momenta above 80 GeV/c, and around the up-down regions of azimuth. The latter two effects are caused by the horizontal separation of the TPC system imposed by the Pb–beam running.

An illustration of the acceptance performance is given in Fig. 2 where rapidity distributions, in transverse momentum bins, are shown for produced and accepted pions in proton+proton events at 158 GeV/c. For central Pb+Pb interactions this means that about 1000 charged particles are detected.

3 The Magnets

Two super-conducting dipole magnets with a maximum combined bending power of 9 Tm at currents of 5000 A are centered on the beam line. Each have a width of 5700 mm and a length of 3600 mm. Their centres are positioned at about 2000 mm and 5800 mm from the target. The magnet yokes are configured in such a way that there is a maximum opening, in the (horizontal) bending plane, at the downstream end. A free gap of 1000 mm between the upper and lower coils leaves room for large volume (TPC) tracking detectors. The coils have a central bore of 2000 mm in diameter and no pole tips are present. This causes field inhomogeneities with the minor components reaching 60% of the vertical component at the extremities of the active TPC volumes. The standard current settings for data taking correspond to full field, nominally 1.5 T, in the first and reduced field, 1.1 T, in the second magnet.

Operation of TPCs in a magnetic field requires either an extremely homogeneous magnetic field precisely aligned with the drift field, or precise knowledge of magnitude and orientation of the magnetic field. The latter requirement applies to the magnet configuration of NA49. Two independent methods for the precise determination of the magnetic field map have been adopted:

- Based on the known configuration and material of the iron yokes and coils, the magnetic field was calculated with the TOSCA code [4].
- Detailed field measurements by means of Hall probes on a three-dimensional grid with 4 cm$\times$4 cm$\times$4 cm spacing [5] have been performed.

In order to cover the entire sensitive region of the detectors, the magnetic field measurements extended over about 16.5 m^3. The unavoidable mechanical and time dependent electrical instabilities of the measurements were corrected by means of reference NMR and Hall probes, as well as redundant measurements at identical positions with different probes. Special care was taken to remedy distortions due to the Planar Hall Effect, which was as high as 10% in certain regions.

A comparison of the calculated field map with the measurements allowed a cross check of the TOSCA calculations and of the correction and calibration procedures applied to the measurements. The field maps obtained with the two methods agree within 0.5%.

4 Beam Detectors and Triggering

The NA49 detector is located in the H2 beam line of the North experimental hall of the SPS. This line transports a fraction of the extracted heavy ion beam or a variety of secondary beams produced from primary protons to the experiment. A set of upstream scintillation or Čerenkov counters and beam position detectors, see Fig. 1, provides precise timing reference, charge and position measurement of the incoming beam particles. Interaction counters and calorimeters downstream of the target allow for triggering on different final state topologies.

4.1 Beam Counters

Minimization of the total detector material in the beam line is a major concern, especially with heavy ion beams. A minimal set of beam counters (see Fig. 1) is therefore used. Standard scintillator material is installed with hadron beams. As the time-of-flight resolution in low-multiplicity events has to rely on a precise reference time, one of the counters (S1, 5 mm thick) is equipped with four photomultipliers directly coupled to the scintillator. In heavy ion running, a quartz wafer of 200 μm thickness replaces this scintillator, yielding good timing and pulse height resolution from the Čerenkov effect.

A thin Helium Gas-Čerenkov counter (S2') has been developed for Pb–beam operation replacing the 2 mm scintillation counter S2 used with hadron beams. A schematic drawing of this counter is shown in Fig. 3, together with the amplitude response to lead ions. The Čerenkov light is reflected by a 25 μm thick, aluminized Mylar foil into a thin-walled Rohacell plastic foam tube internally coated with Aluminium. A Hammamatsu H6125 mesh dynode photomultiplier collects and amplifies the light signal. Additional magnetic shielding around the multiplier allows installation close to the target, in magnetic fields of up to 0.3 T. Two counters have been operated with He path lengths of 50 and 17 cm. The pulse height spectrum, shown in Fig. 3b, has an amplitude resolution of 10%. This allows for a precise discrimination of ion charge down to a few units of charge.

4.2 Beam Position Detectors

The transverse positions of the incoming beam particles are measured in a telescope of beam position detectors along the beam line (BPD-1/2/3 in Fig. 1). These counters are small (3×3 cm^2) proportional chambers with cathode strip readout. Two orthogonal sense wire planes (15 μm tungsten wires with 2 mm pitch) are sandwiched between three cathode planes made of 25 μm aluminized Mylar (Fig. 4). Together with the two external gas envelopes, this yields a total chamber material equivalent of only 125 μm Mylar.

The outer cathode planes are sliced into strips of 2 mm pitch which are connected to the readout electronics, as shown in Fig. 4a. The charge induced on these cathode strips has an rms width of 2.4 mm such that 5 to 6 strips can be used for centre-of-gravity determination. The resulting precision of the beam position extrapolated to the target is 40 μm for Pb and 170 μm for proton beams. This has to be compared to a beam profile with a σ of 0.5 mm and 1.3 mm respectively.

The chambers are operated in Ar/CH_4 80/20 gas mixture with gains of about 10^4 for protons and about 10 for Pb–ions. Typical charge spectra are shown in Fig. 4b, c for proton and Pb–beams. In Fig. 4d the charge separation power is demonstrated using the charge sum signal of all 6 BPD-planes together with the information of the S2 scintillation counter. Fragments up to phosphor, obtained from a 158 AGeV Pb–beam impinging on a 10 mm carbon converter and with the beam line momentum set to 312.8 GeV/c, are clearly visible.

4.3 Interaction Trigger

For hadron beams, interactions in the target are selected by anti-coincidence of the incoming beam particle with a small ($\emptyset$ 2 cm) scintillation counter (S4) placed on the beam line between the two vertex magnets (see Fig. 1b,c). This counter defines a trigger cross section of 29 mb in proton+proton collisions at 158 GeV/c beam momentum, eliminating 80% of the elastic and 50% of the diffractive cross section, both processes being anyway outside the acceptance for particle tracking. This counter had to be placed in a strong magnetic stray field. Its 150 cm long light guide combines an air section inside a thin Rohacell foam cylinder with a wave length shifter bar close to the Hammamatsu H6125 mesh dynode photomultiplier.

For Pb–ion beams, an interaction trigger is provided by anti-coincidence with a Helium Gas-Čerenkov counter of the type described above (S3 in Fig. 1a). This counter actually contains the target and has a length of 17 cm up to the thin reflective Mylar mirror. With a 224 mg/cm^2 Pb–target and the requirement of Čerenkov pulse heights below 90% of the full Pb–ion signal, a selection of impact parameters up to about 10 fm with less than 10% background has been obtained.

4.4 Selection of Central Pb+Pb Collisions

In order to select at the trigger level the few percent of central interactions contained in the target interaction rate, additional information on the energy flux remaining in the beam area is needed. This is achieved by using a Veto Calorimeter (VCAL in Fig. 1) placed about 20 m downstream of the target behind a collimator. The opening of the collimator is adjusted such that beam particles, projectile fragments and spectator neutrons and protons can reach the calorimeter.

The Veto Calorimeter, constructed originally for the NA5 experiment [6], consists of a lead/scintillator section of 16 radiation lengths followed by an iron/scintillator section of 7.5 interaction lengths. The energy resolution can be parametrized by $\sigma(E)/E = 1.0/\sqrt{(E(\mathrm{GeV}))}$. Fig. 5a displays the energy spectrum observed in Pb+Pb collisions at 158 AGeV [7]. Central collisions can be selected by discriminating the analog energy sum signal. A typical threshold setting at $E_{veto} \leq 8$ TeV corresponds to about 4% of the Pb+Pb interaction cross section and an impact parameter below 3 fm as illustrated in Fig. 5b.

4.5 Centrality Detector for Hadron+Nucleus Collisions

The impact parameter in hadron+nucleus collisions is known, from emulsion and bubble chamber work [8], to be correlated to the number of "grey" target protons in the laboratory momentum range 0.15 to 1.0 GeV/c. Detection of and triggering on these slow protons is an important asset in the detailed study of hadron+nucleus phenomena. A centrality detector surrounding the nuclear target has therefore been developed (CD in Fig. 1c).

This detector has the shape of a vertical cylinder with 16 cm diameter and 20 cm height with a thin (about 0.3% interaction length) target placed in its centre. It is a gas detector consisting of 32 proportional tubes read out on 256 cathode elements each covering about 20 msterad solid angle, Fig. 6a. The counter subtends lab polar angles from 45° to 315°, leaving free the tracking acceptance wedge of the NA49 spectrometer.

Protons below 0.15 GeV/c momentum are cut off by range in a cylindrical copper foil between target and proportional tubes, thus eliminating evaporation ("black") protons and nuclear fragments. Detection of protons above about 0.6 GeV/c and pions is progressively suppressed by placing the electronics detection threshold at about three times the most probable energy loss of minimum ionizing particles.

The hit pattern is recorded in latches after threshold discrimination. On-line triggering on the number of produced hits is available via a fast majority coincidence. A typical number distribution of hit cells is shown in Fig. 6b for p+Pb collisions at 158 GeV/c. We have taken data triggered by more than typically 2 and 7 hits in order to obtain high statistics samples also in the tail of this distribution. The acceptance of the counter has been estimated, by comparison with known angular distributions and with events from the VENUS generator, to be about 40% of the produced grey protons. The expected distribution of the number of participants is shown for two trigger thresholds in Fig. 6c, d as calculated with the VENUS model.

5 The TPC Tracking System

5.1 Design Considerations

The fixed-target kinematics at SPS energies is very convenient for tracking with Time Projection Chambers, as the mean particle emission angle at central rapidity is only in the range of 100 mrad (see Fig. 7). The given magnetic aperture therefore contains a large fraction of all produced particles with modest vertical drift lengths of order 100 cm and only small dip angles, with most tracks being almost orthogonal to the electric and magnetic fields.

Sizeable track angles may occur, however, in the bending plane of the magnets. Due to the large transverse momentum kick of 1.5 GeV/c provided by the magnetic fields, particles with opposite charges are cleanly separated into two opposite horizontal hemispheres. Track angles with respect to the beam direction vary from a few degrees in the extreme forward direction at high momentum to a maximum of about 50 degrees for the lowest accepted momenta at around 1 GeV/c in VTPC-1. By adapting the direction of the TPC readout pads to these track angles in the various detector modules, the angle difference between tracks and pads can be kept small. The TPC space resolution can therefore be exploited in the limit given by diffusion only, both in drift and bending direction.

On the other hand, the large particle multiplicities encountered in heavy ion collisions lead to extreme track densities of up to 0.6 particles per cm^2 in the plane orthogonal to the beam direction. Neighbouring tracks tend to run closely parallel over most of their measured track length. The width of the charge distributions in both coordinates transverse to the drift direction has therefore to be kept to a minimum. Gases with low transverse and longitudinal diffusion coefficients (the MTPCs operate without magnetic field) and with moderate drift velocities have to be chosen. The width of the induced charge distribution (pad response function) and the electronics shaping time constants have to be optimized accordingly.

In addition, and again due to the large track densities, charge information from the sense wires of the readout chambers cannot be pattern-recognized. Tracking and energy loss measurements have therefore to be obtained from pad readout only (see Fig. 14). This requires careful optimization of the chamber and electronics operation conditions.

Some information on the geometrical dimensions of the TPC system is given in Table 1.

5.2 Gas Choice

In a preparatory R+D project [9, 10] a number of gas mixtures has been investigated, in particular concerning diffusion coefficients, drift velocities and electron attachment. As demonstrated in Fig. 8, the FWHM of the charge distributions can be limited to about 5 mm both in transverse and longitudinal (drift) direction, if cool gases containing CO_2, combined with narrow pad response functions and drift velocities between 1 and 3 cm/μs are used. This represents a sizeable improvement over the Ar/CH_4 mixtures especially in drift direction and for applications without magnetic field.

Our final choice has been a mixture of Ne/CO_2 (90/10) for the VTPCs and of $Ar/CH_4/CO_2$ (90/5/5) for the MTPCs. Diffusion coefficients have been measured to be 220 $\mu m/\sqrt{cm}$ and 270 $\mu m/\sqrt{cm}$ respectively, for the two gases, in both transverse and longitudinal direction. Drift fields of 200 V/cm (175 V/cm) correspond to drift velocities of 1.4 cm/μs (2.4 cm/μs) in the two types of detectors. In this range, drift velocities are unsaturated, i.e. they change almost linearly with electric field. The exact measurement and control of drift velocity and its correction for pressure and temperature variations therefore becomes a key issue.

Another peculiarity of gas mixtures containing CO_2 is a relatively strong electron attachment in the presence of Oxygen, which is more than one order of magnitude bigger than in the standard mixtures containing CH_4. We have measured attachment coefficients of 240 (120) per

dimensions [mm]	VTPC-1	VTPC-2	MTPC-L/R	wire material
width	2000	2000	3900	
length	2500	2500	3900	
height	980	980	1800	
drift length	666	666	1117	
pad length	16, 28	28	40	
pad width	3.5	3.5	3.6, 5.5	
pad angles	12–55°	3–20°	0°, 15°	
pad/sense wire dist.	3	2	2, 3	
sense wire diam.	0.02	0.02	0.02	W-Re (gold plated)
sense wire spacing	4	4	4	
field wire diam.	0.125	0.125	0.125	Cu-Be (gold plated)
field wire spacing	4	4	4	
Frisch grid wire diam.	0.075	0.075	0.075	Cu-Be
Frisch grid wire spacing	1	1	1	
gating grid wire diam.	0.075	0.075	0.075	Cu-Be
gating grid wire spacing	1	1	2	

Table 1: Geometrical dimensions of the TPC system.

microsecond and atmosphere of Oxygen, for the two gases quoted above revealing a linear dependence on the CO_2-content. This leads to attachment charge losses of 1.2% (0.6%) per ppm of Oxygen over the 50 μs drift time in the TPCs. Severe constraints on gas purity and leak rate have obviously to be imposed.

Attachment due to water impurities could not be observed up to water contents of several 100 ppm. The dependence of drift velocity on water is also comparatively low, it has been measured to be –2% per 100 ppm H_2O.

5.3 Gas Systems and Monitoring

The detector gas is supplied by four independent gas systems. Each system recirculates the gas with a compressor at a rate of about 20% detector volume per hour, i.e. 0.6 and 4.0 m^3/h for VTPCs and MTPCs, respectively. Flow control is achieved by regulating the TPC overpressure to 0.50 ± 0.01 mbar via frequency modulation of the recirculation pumps. A schematic drawing of one gas system is presented in Fig. 9.

Fresh gas is mixed and fed into the recirculation system through mass flow controllers [11] which can deliver, in purge mode, the full recirculation rate. In normal operation, the fresh gas is supplied at only 2% detector volume per hour. Nonlinearities and calibration drift of the flow controllers are eliminated by on-line control of gas amplification and drift velocity, as the required setting accuracy is beyond the specifications of the flow regulators. The mixing and monitoring equipment is temperature stabilized to better than 0.1°C. Oxygen is cleaned from the detector gas by filter columns containing active Cu-granules chosen for use with the CO_2 gas mixtures. No absorption or exchange of CO_2 with the other gas components or water has been observed. The filters are regenerated after typically 4–6 months operation periods, using Ar/H_2 (93/7) mixture at 200°C. Fresh filters absorb water contamination in the gas over periods of some weeks, such that the water content may vary by 10 to 20 ppm.

As mentioned above, the control of gas quality is one of the major issues in the NA49 TPC system. Oxygen and water contaminations are measured with two pairs of O_2/H_2O sensors

[12]/[13] which can be switched to different positions in the recirculation systems (B,C,D,G in Fig. 9). Gas purities of 2–4 ppm Oxygen and about 20 ppm water are typically achieved.

Owing to the required dE/dx performance and space resolution in drift direction, and due to the large time constants (50 hours per volume change) involved in the propagation of gas instabilities, the gas mixtures have to be stabilized to a very high level of accuracy. We achieved a relative stability of better than 0.5% in gas gain and a measurement of drift velocity to better than 0.1% absolute and 0.03% relative.

Each of the gas systems has a system of four gas amplitude monitors and one drift velocity monitor. The amplitude monitors measure the signal from ^{55}Fe photons in a proportional tube, both in the fresh gas input line and in the recirculated gas. Pressure and temperature variations are corrected up to quadratic terms in gas density. Drift velocity is measured in a drift detector using the drift time difference from a pair of Alpha sources at 10 cm distance [14]. Typical performances and precision of these monitors are shown in Fig. 10 for a period of several weeks [15]. It should be stressed that in three component gas mixtures as used for the MTPCs, both gas gain and drift velocity have to be measured in order to control the relative concentration of the gases.

5.4 Field Cages, Gas Envelopes and Support Plates

The design of the field cages has been guided by the following criteria:

- no insulator surfaces exposed to the drift volume
- single-layer electrostatic field structure
- functional separation of field cage and gas envelope
- outside protective gas volume for gas purity and HV safety
- minimization of overall material thicknesses
- modular construction for ease of assembly and avoiding large and complex auxiliary structures
- 100 μm geometrical precision of all field cage elements over the full volume.

These considerations led to the realizations described below.

5.4.1 Field Cages

The basic elements for the electrostatic field electrodes are aluminized Mylar strips of 25 μm thickness and 1/2 in width. If stretched with a load of about 1 kg they can be suspended over a length of 150 cm with a vertical sag of less than 50 μm (if on edge) or 170 μm (if flat). This load corresponds to an elastic elongation of 0.7%. This is far below the deformation limit. Test strips have shown creep of less than 20% of initial elongation over a period of 5 years. Humidity has a strong influence on the elongation. A variation from 20% to 60% relative humidity in air increases the elongation by typically 10%. In this sense the exposure of the strips –once mounted– to the dry detector gas provides a welcome contraction balancing eventual small creep effects.

The Mylar strips are suspended on ceramic tubes placed vertically in the corners of the rectangular field cages, with a distance of 2 mm between strip edges. The tubes are pressure-moulded from Alumina [16], surfaced to perfect cylindricity and metallized under vacuum with a Ti layer of about 100 Ω/square sheet resistance. Insulating rings of 2 mm width and 200 μm depth are machined into the tube surface achieving excellent strip-to-strip retracted insulation.

The strips are cut to 99.3% of their suspended length such that the internal elastic force is obtained by elongation on their supports. Each strip is sandwiched at both ends with 100 μm thick Cu-Be material. The metal is tightly bent three times to form a small hook which fixes the strip by friction and at the same time ensures the necessary double-sided electric contact. Both

ends of each strip are hooked onto a fibreglass-epoxy profile placed at the outside of one of the corner tubes (see Fig. 11). The strip position can be adjusted by eye to match the machined strip pattern on the tube surfaces, readily achieving a 50 μm positioning accuracy. The winding of a complete field cage (about 70 strips) can be performed in a working day.

In order to keep the total weight of the field cage structure to a minimum and to meet the required geometrical precision over surfaces of up to 16 m^2, the High Voltage planes are realized using the same type of Mylar strips. Strips are here suspended horizontally between two rows of adjustable wedges and supported every 70 cm on support wires (200 μm Cu-Be) which in turn are supported by adjustable screws. The resulting system of about 100 support points is brought into place with a precision of better than 100 μm using an optical level reference, before placing the strips. This is again a very fast operation. A schematic drawing of the field cage of a VTPC is shown in Fig. 12 [17], while a view inside one of the large field cages for the MTPCs during assembly is given in Fig. 13.

5.4.2 Gas Envelopes

As stated above, the gas envelopes are completely separated from the drift field structure. They consist of a double layer of 125 μm Mylar foil glued to a double frame system made of 6 mm thick fibreglass-epoxy. The thin (1–2 cm) gas volume between the two foils is flushed with Nitrogen and serves the double purpose of High Voltage protection and minimization of gas impurity diffusion, especially concerning Oxygen and water.

The severe constraints on gas purity imposed by the use of CO_2 as drift gas necessitate optimum assembly and gluing techniques in the preparation of the gas boxes. A length of more than 100 m of glue joints per detector has to be produced in the assembly process, using Araldite [18] throughout. With this type of glue, careful wetting and humidity control combined with visual inspection proved sufficient to reach the necessary gas purity performance, without any need for leak searches.

5.4.3 Support Plates

Both the field cages and the gas envelopes are carried by support plates which also house the readout proportional chambers. In the case of the VTPC detectors, the plates of 250×200 cm^2 are machined from solid Al of 145 mm thickness. They are supported from 4 points on the magnet iron. After careful horizontal alignment of the support points, they present a reference surface of $\pm$ 50 μm planarity. After mounting the Ceramic rods and the HV support structure, the field cage is assembled by winding the Mylar strips. The gas box is then fixed to the support plate using a simple system of clamps. Gas tightness at this joint is ensured by room temperature vulcanizing paste, RTV [19]. Comparative leak rate tests have shown that this rubber is equivalent to standard O-ring joints which need precision surfacing and the application of high mechanical forces. Since RTV contains Silicon, careful ageing measurements [20] have been performed in order to prove that no sense wire ageing is induced. This is true if perfect volume polymerization is ensured by using RTV only for joints exposed to air and by strictly limiting its bulk volume to a few mm cross section. This technique also allowed substantial simplification of the readout chamber mounting in the support frame by replacing O-ring joints with RTV seals.

For the MTPCs with their 16 m^2 top surface, the support frame has been realized as a complex mechanical assembly of 40 cm height using a combination of screw and glue junctions on preassembled subsections. Planarity is achieved by machining the lower surface after assembly. The plate is supported on 4 points. This again calls for careful alignment of the structure presenting a total weight of 5.5 t. A surface planarity in situ of $\pm$ 150 μm has been achieved.

The weight of the gas box and field cage, both acting on the circumference, is a major factor in this deformation. The gas box is therefore again held with simple mechanical clamps and the gas tightness ensured with an RTV seal. In the case of the MTPCs, the readout modules are fixed from below the frame in order to allow for a relative separation of only 2 mm. The gas seal is realized with O-rings.

5.5 Readout Chambers

The NA49 TPC system deploys 62 readout proportional chambers each with a 72×72 cm^2 detector surface. The chambers are constructed using the classic design developed over many years of TPC technology [21, 2]. Seen from the drift space, a gating grid is followed by a cathode plane (Frisch grid) closing the proportional chamber volume made up by 20 μm sense wires interspaced with 125 μm field (zero potential) wires. Signals are picked up on the back cathode plane which is subdivided into pads. A selection of principal dimensions is given in Table 1. A cross sectional view is shown in Fig. 14.

Several points are noteworthy in the NA49 realization:

- small gaps between pads and sense wires (down to 2 mm only [10]) in order to adapt the width of the induced charge distribution (pad response function) to the small FWHM of the drifted ionization charge (Fig. 8). This allows full use of the possible space resolution and two track separation.
- consequently, small pad widths down to only 3 mm leading to very high electronics density of up to 4000 channels per readout module.
- adaptation of pad length and angle to track topology in the various detector areas to minimize track angle effects.
- excellent gas tightness by covering the pad contacting holes with an auxiliary plate and displacing the back electronics connectors with respect to the pad rows. Leak tightness of each module was measured on a He test stand requiring a He leak rate of less than 10^{-6} mbar·l/s.
- direct connection of front-end electronics cards on the chamber back plane in groups of 32 channels per card.
- metallic support frame machined from a 60 mm thick Al plate carrying pad and wire planes as well as electronics cards and cooling system.
- pad plane made from a printed circuit board (PCB) glued to the Al frame. The pad pattern is first transferred to a glass plate in order to keep the required mechanical tolerances and this mask is then used to etch the pad pattern on the PCB [22].

Due to the good noise performance of the electronics, the chambers can be run with a gas gain of only $5{\cdot}10^3$ in the MTPCs. This is of paramount importance for the stable operation at large track density. Due to shorter pad lengths and low density gas, the gas multiplication in the VTPCs is increased to $2{\cdot}10^4$. The corresponding chamber currents during the SPS spill are of order 100 nA in the high track density area of the MTPCs and up to 500 nA in the VTPCs. These currents correspond to direct track load through the effective chamber volume between gating grid and pad plane, the contributions from track segments drifting in during the gate opening time being negligible. Although the transition to breakdown is rather rapid in Ne gas mixtures, no operational problems have occured in the VTPCs in four years of running. In contrast, there is a tendency of self-stable discharges developing in the MTPC modules closest to the beam.

5.6 Electronics

The TPC readout system comprises a total of 182000 pads. The corresponding electronics system represents a complexity and channel density that can only be handled by making use of

VLSI full custom technology. The electronics design had to satisfy the following criteria and boundary conditions:

- signal sampling frequency 10 MHz corresponding to 512 time buckets over the maximum drift time of 50 μs
- system dynamic range 8 bits
- equivalent noise charge about 1100 electrons (rms)
- signal shaping time of 180 ns, adapted to longitudinal diffusion

These led to the following technical realizations:

- analog signal storage in Switched Capacitor Arrays (SCA)
- digitization in Wilkinson-type ADCs with 9 bit resolution
- placement of complete front-end electronics up to digital outputs on the TPC readout chambers
- digital data transfer via optical links
- high degree of multiplexing to reduce number of links
- digital signal processing in a VME based system of receiver boards performing zero suppression, multi-event buffering, and data transfer to event builder

The design follows a readout structure first developed for the EOS experiment [3] and also adopted by the STAR collaboration [23]. Its function is based on a low event recording rate of 10–30 per SPS burst and on the absence of higher level trigger decisions requiring fast intermediate buffering. Efficient minimization of the number of components and a high degree of multiplexing are thereby possible even keeping in mind the very large raw data volume of 100 Mbyte per event. A detailed description of the electronics can be found in [24].

5.6.1 Front-End Electronics

The complete front-end electronics is grouped on 32 channel cards which are connected to the corresponding pads on the back plane of the readout chambers. The main components are highly integrated into two types of custom designed chips: a 16 channel preamplifier/shaper and a 16 channel analog storage/analog-to-digital converter, both realized in CMOS technology [25].

The preamplifier features an input integration circuit with a 1.5 pF feed-back capacitor and a conversion gain of 50 mV/fC. The capacitor is discharged via a FET switch such that charge accumulation is active only during drift time under control of the event trigger. The total dynamic range of the input stage is 12 bit corresponding to a charge deposit of 40 minimum ionizing particles on the pad. A subsequent shaper stage forms the signal into a Gaussian wave form with 240 ns FWHM. The power consumption of this chip is 53 mW/channnel. The equivalent noise charge in running conditions is 1500 electrons.

The analog pad signal is time-sampled and stored in a Switched Capacitor Array (SCA) [26] which can be regarded as a series of 512 capacitors with a sample and hold circuit for each capacitor. After the readout cycle of 50 μs, the stored charges are transferred with a frequency of 100 kHz to a Wilkinson type ADC using a single slope ramp and counter with 9 bit resolution. The power consumption of this chip is 5 mW/channel.

5.6.2 Data Transfer and Processing

The digitized information is transferred by flat ribbon cables to Control and Transfer boards also located on the TPC support plates. Here data are multiplexed and sent to the counting house on fibre optical links with a speed of 62.5 MHz. 768 electronics channels are multiplexed onto one fibre.

Receiver boards (3072 channels per board) mounted in a VME crate system perform digital data processing tasks including pedestal calculation and storage, zero suppression, noise rejection and event buffering, using Motorola DSP 96000 processors. In this stage the data volume is compressed to less than 10% of its raw volume such that one complete event corresponds to about 8 Mbyte of data for central Pb+Pb interactions.

5.6.3 Cooling and overall Temperature Control

The power consumption of 58 mW per channel, combined with the large channel density, leads to thermal loads of up to 300 W per readout chamber. As the required temperature stability of the detector gas is of order 0.1°C for gas gain and drift velocity control, a recirculation water cooling system was designed. This system uses permanent underpressure of the whole circuit in order to prevent water leakage into the TPC environment [27]. The system consists of Cu cooling plates installed in between the electronics front-end cards, a vacuum pump with expansion vessel, a heat exchanger and a circulation pump. System temperature is stabilized by microprocessor control of the heat exchanger valves.

Overall temperature control of the detector system is achieved by regrouping the complete VTPC and Laser systems on one hand, and the MTPC and TOF systems on the other hand in two large thermally insulated huts connected to two high precision climatizers. By a combination of cooling and subsequent processor controlled heating the ambient temperature is stabilized to 20 ± 0.1°C. Temperatures are monitored by 60 PT–100 thermal resistors.

5.6.4 Performance

The electronics system has performed in a very stable and reliable fashion over the past four years. During this period of order 1% of the 6000 front-end cards had to be exchanged due to malfunction of single channels or chips. The production yield of the 16 channel chips (about 200 mm^2 silicon surface) has turned out to be about 50% after detailed dynamic acceptance testing for a series of key parameters on computer-based test stands. Channel gain and shaping time have Gaussian distributions with about 10% rms.

The typical pulse shape from a laser track in a MTPC is presented in Fig. 15. The signal shows a good Gaussian symmetrization, with a short-term undershoot of about 5% affecting the base line up to about 1 μs (corresponding to a space dimension of several cm) in the neighbourhood of each track (Fig. 15a). At larger times, the signal is followed by a complex overshoot/undershoot structure on the level of less than 0.5% (Fig. 15b). These features are connected to the principle of pad readout and are not taken out by the shaping stage since the necessary long time constants cannot be realized in VLSI techniques. As practically no positive ions arrive at the pad plane, the time integral over the signal has to be zero. Hence a negative undershoot occurs which starts at about 5 μs and continues beyond the TPC open time. In high track density environments, this undershoot results in a base line shift due to tail superposition which looks like an effective charge loss as function of drift distance. In central Pb+Pb collisions this effect may reach several percent of the mean pulse height, thus affecting the quality of dE/dx determination. Off-line corrections have been developed in order to remedy this situation.

Another observation, again depending on track density, concerns changes of both channel gain and base line position depending on the input charge load on each chip. This has to do with the difficulty of proper channel decoupling in a high component density VLSI environment. As a result, the apparent channel gain can vary by up to 10% depending on the pattern of the input charges on each chip, and on the chip position on the front-end cards. This precludes the possibility of performing electronics calibration using pulsing of the field wires, as in this case

all channels of a full readout module are loaded simultaneously. Alternative methods of gain calibration had to be developed (see below).

The feedback capacitor of the preamplifier has a 12 bit dynamic range. In some instances this capacitor can saturate in the high track density areas of the detector leading to an abrupt loss of charge measurement for times beyond the saturation point on the affected channel.

5.7 Data Acquisition

The data flow of 100 Mbyte per event from the front-end electronics is transferred through fibre optical links to 60 receiver boards (4 fibres or 3072 pads per board) housed in a system of 6 VME(9U) crates. These act as slaves to a VME(6U) master crate which steers all the data acquisition. It is controlled by a master processor based on the Motorola 68040 CPU with master/slave and VSB/master interfaces. The master crate contains seven 32 MByte dual-ported VME/VSB Micro Memory modules (DPM) which are used to contain event fragments during the readout process. The principal layout of the sytem is given in Fig. 16. The event rate is 25–30 per SPS burst (4.8 s for Pb–beam, 2.37 s for p–beam).

In addition to the TPC data transfer, the master crate receives data from several CAMAC branches (beam, trigger, calorimeter and PesTOF information) and from a FASTBUS system (Time-of-Flight information) connected through a FASTBUS AEB master (ALEPH Event Builder).

After all event fragments have been transferred to the 32 MByte memories in the master crate, a complete event is assembled by the master CPU in its local memory. An event can then be transferred either to 8 mm Exabyte tapes for test purposes, or, in production running, via a VME-SCSI2 interface to a SONY DIR-1000M 19 mm tape recorder which can operate at a transfer rate up to 16 MByte/s. The recorder is driven by a SCSI2 controller [28] which manages all aspects of the tape operation. Transfer to the SONY controller can be maintained in excess of 16 MByte/s so that the drive operates in streaming mode. The capacity of the largest tape cassette is 100 GByte which corresponds to about 100 min of uninterrupted running or in excess of 10000 events on a single tape (central Pb+Pb interactions). Events may also be transferred via FDDI to UNIX work stations for online monitoring.

All the VME processors run under the OS9/68000 operating system. Booting and file serving is done via a UNIX workstation. The DAQ software in the master CPU is organized as a set of different concurrent tasks and has been described in detail in [29]. Almost all of the software is written in C++, a language which makes it conceptually easy to communicate with hardware and shared objects through access functions. The system takes approximately 85 ms to assemble a single event and transmit it to the tape controller.

5.8 Calibration

Simultaneous calibration of electronics and gas gain can be achieved by releasing a known number of electrons into the TPC drift space. Injection of radioactive ^{83}Kr gas can serve this purpose. This method has been developed by the ALEPH collaboration [30] and is being used by the DELPHI experiment [31] for similar application.

The unstable ^{83}Kr isomeric state (half life 1.9 hr, excitation energy 41.6 keV) emanates from a ^{83}Rb source [32] housed in a small volume by-pass of the TPC gas recirculation system and is injected into the TPC gas. This isomeric state decays to the ^{83}Kr ground state through an excited state at 9.4 keV. Both the 32.2 keV and the 9.4 keV nuclear deexcitations are dominated by internal conversion transitions and the subsequent atomic deexcitations are dominated by Auger transitions. Escapes of the 9.4 keV gamma-ray and of the 12.6 keV to 14.3 keV X-rays from the decay site in the TPC gas produce a characteristic spectrum of electron deposition

at the decay site which has peaks at 19.6, 27.3, 29.0, 32.2, and 41.6 keV. In the large TPC volumes the escape photons are converted with full efficiency. The resulting charge distribution is shown in Fig. 17a for a Monte Carlo simulation using the known transition probabilities, and compared in Fig. 17b to a measured spectrum in one of the MTPCs. As the lowest peak at 9 keV is close to the MIP equivalent of 6 keV in the MTPC, this method offers, in addition to relative gain calibration, a precise check of detector and electronics linearity up to 7 times minimum ionization.

Calibration data are taken with a clock trigger at maximum data acquisition rate. For a source intensity of 180 MBq, about 1000 Kr decays are captured in a single readout cycle of 50μs. In a data taking period of about 2 hours, this permits the production of high statistics charge spectra on the level of 16 pads (or one readout chip) grouped together. Owing to its short decay time constant, the radioactive component will vanish quickly and normal data taking can resume after some hours.

The more than 10^4 charge spectra established by this procedure are fitted automatically by comparison with a reference spectrum using the full information contained in the method, yielding a precision of better than 0.5%. It has thus been possible to remedy the electronics calibration problems mentioned above and at the same time to take out the systematic variations of the gas gain which can reach 10% over the readout chamber surfaces.

Kr calibration runs are typically taken before and after each SPS running period of 6 to 8 weeks. The time evolution of the detector response in the intermediate time period has been shown to be uniform over each of the 62 readout modules, and to be determined mainly by pressure variations and setting uncertainties of chamber HV and electronics LV supplies. This time dependence is traced by pressure correction up to second order in gas density and by following the time dependence of particle energy loss, via truncated means of several thousand charge clusters per readout module, with an accuracy of better than 1%.

5.9 Detector Geometry, Alignment and Track Distortions

The space position of the TPC system is determined to better than 200 μm absolute accuracy, by optical methods. Fiducial marks on each detector are brought into relation with the exterior SPS beam coordinates using precision survey methods [33]. The relative positions are controlled, in short time intervals, by level instruments [34] for the vertical coordinates and by vertical optical reference lines [35] for the horizontal ones.

Internal consistency is checked with muon tracks and multi-target runs. High momentum muons from the secondary beam halo are available in abundance. They pass, parallel to the beam, through sets of three subsequent TPCs (see Fig. 1) and offer perfect long-baseline alignment. Secondary tracks from additional targets placed upstream and downstream of the primary one provide cross checks of angle effects, left-right asymmetries and vertex precision.

The basic detector geometry is first determined without B field in the vertex magnets. In this condition, the internal consistency between survey constants and track positions is found to be better than 200 μm, in the horizontal coordinates. The determination of the vertical coordinates needs, in addition to absolute detector position, absolute measurement of drift velocity and readout time reference. The drift velocity is predicted from the drift velocity monitors (section 5.3) using atmospheric pressure, gas temperature, and TPC drift field measurements. The time reference is determined independently from multi-target runs using the vertex constraint from the beam position detectors (section 4.2). Both measurements are independently not precise enough to guarantee the requested absolute position accuracy of 200 μm in the detector midplane (corresponding to a precision of $4{\cdot}10^{-4}$) in drift velocity and 8 ns in reference time. Small adjustments of the drift velocity are therefore applied in order to obtain an overall optimization

of the global track residuals between the different TPCs using the vertex constraint.

In an alternative way the drift velocity can be determined by laser tracks or via the charge distribution inside each TPC as a function of time (called charge step method). The determination with laser tracks requires high absolute precision in position and angle of each track in the TPC volume, which turned out to be difficult to guarantee. The charge step method is based on a fit to the back edge of the charge distribution of tracks corresponding to the position determination of the drift HV plane (in time). As such it is well suited to the high track and charge density environment of heavy ion collisions, where it achieves an excellent relative precision of about 10^{-4} in an event-by-event measurement. For the absolute drift velocity determination it necessitates the knowledge of the readout time reference, the transition time in the readout chambers, and a correction for cluster charge distortions close to the HV plane which are difficult to evaluate.

The above mentioned residuals used for the adjustment of the drift velocity suffer in addition from track distortion effects specific to each TPC. Two main sources of track distortions have been found: the transition region between drift space and readout chambers, and the $E \times B$ effect in the magnetic field. Due to the complex electric field geometry in the edge regions of the readout chambers (isolating frames, gaps between chambers) it is virtually impossible to obtain a perfect match between the drift region and the volume around and below the gating grids. Local charge displacements of more than 100 μm in all three coordinates are observed. These displacements show up as drift-independent quantities and have to be taken out by correction tables.

The large magnetic field inhomogeneities in the vertex magnets (see section 2) lead to very appreciable displacements of the drifting charge which reach several cm at the edges of the VTPCs. These effects have therefore to be known with precisions of about 1% of their value. Due to the low $\omega\tau$ values of the cool gases used in our experiment, rather precise predictions are possible using the measured B fields and drift velocities. Experimentally, the availability of laser tracks over the complete volume of the VTPCs (see next section) allows for a perfect cross check of the validity of these predictions. The $E \times B$ distortion can thus be eliminated with the necessary precision.

5.10 Laser System

The NA49 laser system is based on a pulsed Nd-YAG laser [36] equipped with 2 frequency doublers and delivering a power of 4 mJ per pulse at a wave length of 266 nm. The laser beam can be directed with an automatic steering system towards any one of the four TPCs. There it is split and directed vertically down into the ceramic support tubes placed in the corners of the field cages, see chapter 5.4.1. Auxiliary ceramic tubes inside these columns carry 6 beam splitters at 45 degree angle which reflect the pulse, through Quartz windows, into the TPC drift volume. The auxiliary tubes can rotate in steps of 3 degrees driven by a pneumatic precision stepping mechanism. Beam positions are recorded and stabilized via position sensitive laser diodes (PSD) and autocollimation using steering with stepping motors and piezoelectric tripods. The schematic layout of one laser beam system is shown in Fig. 18a. Laser beams in up to 200 precisely defined positions can thus be produced, spanning the entire TPC volume.

The laser system has been successfully used in the study of tracking performance and all kinds of track distortions. In particular, it has been indispensible for the control of the large $E \times B$ distortions mentioned above, and their correction. Residual distributions with respect to straight line fits in horizontal coordinates are shown in Fig. 18b, c, without and with the calculated $E \times B$ corrections.

6 Tracking Method and Performance

The NA49 track reconstruction software is structured into several consecutive steps:

1. cluster finding
2. construction of local track elements in each TPC separately
3. matching of track elements from different TPCs into "global" tracks
4. track fitting through the magnetic field and momentum determination.

In the first step, two-dimensional charge clusters are formed by grouping information from neighbouring pads and time buckets in each pad row (pads are arranged orthogonal to the beam direction in 72 rows per VTPC and 90 rows per MTPC). The position of each cluster is found by centre-of-gravity formation over the charge distributions. For matched global tracks a minimum of 10 clusters is requested, a possible maximum being 234 clusters. The distribution of the number of clusters per track between these limits is shown in Fig. 19. It is determined by the production kinematics of tracks at vertex, combined with the momentum dependence of magnetic deflection. In the distribution of Fig. 19, enhancements at about 50 clusters (single VTPC), 80 clusters (MTPC only) and 150 (one VTPC+MTPC) are visible. Evidently, the achieved momentum resolution will show a variation corresponding to track length and magnetic field configuration traversed by the track.

6.1 Residual Distributions and Space Resolution

Typical residual distributions, with respect to track fit, are shown in Fig. 20 for muon tracks without B field and for tracks from p+Pb interactions with B field, in vertical and horizontal coordinates. It should be stressed that only geometrical and $E \times B$ corrections have been applied. Thus the electric field distortions near the readout chambers described in section 5.8 are fully visible, especially in the vertical coordinate. From the size of the systematic residual effects we conclude that an overall position precision of about ± 200 μm has been achieved.

From the width of the residual distributions in each pad row we can deduce the local space resolution of the detector. The σ^2 of this distribution in the bending plane is shown in Fig. 21 as function of drift length in the MTPC, for muon tracks. The achieved space resolution varies from 120 μm close to the readout chambers to 270 μm at maximum drift length, an average characteristic value being 210 μm at mean drift distance. One should remember here that this TPC works outside the magnetic field.

The build-up of this performance from the different sources of fluctuations has been studied in detail using Monte Carlo techniques and compared to the usual cumulative formula [21], neglecting angle effects which are small in this case:

$$\sigma^2 = \sigma_0^2 + \frac{\sigma_{\mathrm{diff.}}^2 \cdot L_{\mathrm{drift}}}{N_{\mathrm{el}}^{\mathrm{tot}}} \tag{1}$$

The expected resolution from the diffusion term of this parametrization alone is indicated as the full line in Fig. 21. Evidently the expected drift length dependence does not comply with the data, which are represented by full circles. Comparison with the Monte Carlo calculation (open triangles) reveal that gas gain fluctuations of the avalanche formation at the sense wire contribute exactly a factor of 2 to the diffusion term (hatched line in Fig. 21).

The other principle source of fluctuation is the σ_0–term which is of order 120 μm in this experiment. We have shown that this term originates mainly from finite pad size, electronics noise and from the zero suppression threshold, each with roughly the same contribution. In fact in NA49 the electronics noise (σ) corresponds to 2–3 ADC channels. Therefore the zero suppression threshold has to be placed at 5 ADC channels reducing the effective dynamic range. The most probable charge deposit of minimum ionizing particles has been adjusted to 60 ADC channels which is only 12 times the zero suppression threshold. Therefore the σ_0–term becomes

relatively important. In addition, since the amplitude depends on the drift-length, it is not constant. This introduces an additional drift dependence of the resolution which is also apparent in Fig. 21. Taking these results into consideration equation (1) has to be reformulated as follows:

$$\sigma^2 = \sigma_0^2(L_{\rm drift}) + 2 \cdot \frac{\sigma_{\rm diff.}^2 \cdot L_{\rm drift}}{N_{\rm el}^{\rm tot}} \qquad (2)$$

6.2 Momentum Resolution

The momentum resolution in the bending plane is mainly governed by the local coordinate resolution, the length integral of the magnetic induction, the total track length and the number of measured coordinates on a track [37]. An additional momentum-independent offset due to multiple Coulomb scattering in the target, in several gas layers and in the materials (Al, Mylar) forming the detector walls has to be added; it amounts to less than 3 MeV/c.

Given the wide variation of track lengths and number of points measured per track (see Fig. 19), a general parametrization of momentum resolution (especially in the momentum components) cannot be given. Typical values for the total momentum resolution are dp/p^2=7.0·10^{-4} (GeV/c)$^{-1}$ for tracks passing through VTPC-1 only (momentum range 0.5–8 GeV/c), and dp/p^2=0.3·10^{-4} (GeV/c)$^{-1}$ for so-called global tracks detected in VTPC-2 and one MTPC (momentum range 4–100 GeV/c).

6.3 Primary Vertex Resolution

The position of the primary event vertex is constrained in the plane transverse to the beam with a precision of a few hundred microns by the measured beam particle trajectory (section 4.2). Its longitudinal position has to be obtained by extrapolation of secondary tracks to about 80 cm upstream of the first VTPC. Vertex position is of importance for the separation of secondary decay vertices (neutral strange particles and photon conversions), and for the elimination of background tracks and events originating in the target walls (p+p and p+Pb interactions). In high multiplicity events, the vertex resolution is of order 150 μm in the bending plane as shown in Fig. 22a for central Pb+Pb interactions without using the beam particle position. In low multiplicity topologies, the beam trajectory has to be used as a constraint. In these cases, the resolution (σ) along the beam axis is of order 6.4 mm, as shown in Fig. 22b for p+Pb interactions.

6.4 Two-Track Resolution

The separation of pairs of close, neighbouring tracks is a major concern in the high track density regions of Pb+Pb interactions. The problem is compounded in fixed-target geometry by the fact that most tracks tend to be parallel over most of their length in a given TPC, as only a minority of tracks cross each other with large angles. The spatial distance has therefore to be defined as a mean distance over track length, measured in several points.

As explained in section 5.2, the gas mixtures and detector parameters have been chosen in order to obtain track charge distributions with typically 5 mm FWHM. Separation of tracks down to about 1 cm distance should therefore be possible. The two track resolution has been experimentally determined by comparing the spatial distance of track pairs in the same event with a combinatorial background of pair distances obtained by mixing uncorrelated tracks from different events. This separation efficiency is shown in Fig. 23 to decrease to 50% at an average distance of 1 cm, in agreement with expectation.

Separation below this typical distance is in principle possible using deconvolution techniques developed for the NA49 detector [38]. From these studies it appears that full separation might be possible down to the level of 3–5 mm mean distance, if dE/dx information is included.

6.5 Tracking Efficiency

The TPC concept with its three-dimensional charge cluster measurement guarantees in general excellent track finding efficiency. In the NA49 environment there are two limiting conditions which can lead to track losses: high track density areas where clusters start to merge and therefore get lost for pattern recognition, and tracks ”on the wrong side” with respect to the magnetic bending. Although the majority of tracks separate into two opposite horizontal hemispheres following their charge, tracks with sizeable transverse momentum can reach the ”wrong” hemisphere of charge. These tracks have large crossing angles with respect to the pad pattern designed for ”right” side tracks and therefore create extended clusters which tend to split due to their low charge deposit per pad. The corresponding losses are concentrated at low total momentum in an area where the detector acceptance is low anyway.

In reactions with low multiplicity, the human eye can be used to measure tracking efficiency quite effectively by eye-scans. Tracking efficiencies very close to 100% have been found in p+p and p+Pb interactions, with the exception of a small phase space region at low momentum discussed above.

In the high multiplicity final states produced in Pb+Pb collisions tracking efficiency is determined by embedding Monte-Carlo generated tracks into real events and then measuring the reconstruction efficiency of these additional tracks. This efficiency, which is in general found to be higher than 95%, can drop to about 30% in the regions of high track density close to the beam (see Fig. 24a). This can be correlated to the high electronics occupation density which can reach values of 30% in these areas, as shown in Fig. 24b, c.

Equally problematic for physics analysis are tracking efficiencies above 100% caused by ghost tracks. There are several sources for additional tracks found by the pattern recognition algorithms. The merging of track elements from different TPCs can fail and thus produce split tracks very close to each other in phase space. Considerable effort has been spent to detect and eliminate such cases, which is again increasingly difficult with increasing track density. Another source of additional tracks are secondary vertices. These can be connected to particle decay (V_0's) or interaction of event-correlated particles like neutrons or nuclear fragments in the detector environment, or to pile-up of several events during TPC open time. In all these cases, since these tracks have to match the primary vertex both in elevation and in the bending plane, an accumulation in a small, well-defined area of phase space close to the horizontal plane and at sizeable transverse momenta ”on the wrong side” is found, where fiducial cuts can eliminate them.

7 dE/dx Performance

The precision measurement of specific energy loss and its use for particle identification is one of the principal design goals of the NA49 tracking system. Since the momentum distribution of reconstructed tracks varies from a few hundred MeV/c up to about 100 GeV/c, this measurement spans the full range of the energy loss function from the sub-relativistic $1/\beta^2$ dependence for kaons and protons through minimum ionization into the relativistic rise and up to the Fermi plateau for pions and electrons. In order to keep full flexibility for identification in these different regions, each track is characterized, irrespective of its length, by its proper dE/dx value obtained from a truncated mean over the number of measured charge clusters.

7.1 Calibration

In addition to electronics and gas gain calibration described in section 5.8 above, charges have to be corrected for local track angles and for a small systematic dependence on track length introduced by truncation, which is of order 1%. Since a large number of tracks have points

measured in the different gas mixtures of the VTPCs (Ne/CO_2) and the MTPCs ($Ar/CO_2/CH_4$), the slight differences between the respective Bethe-Bloch functions have been measured and are corrected for, such that "global" energy loss values can be established making full use of the maximum information available for each track.

7.2 Drift Length Dependence of Cluster Charge

The biggest correction is introduced by an important observed drift length dependence of track charge. Only a small part of this charge loss is due to electron attachment, about 1–2% in the MTPCs and 3–4% in the VTPCs (see section 5.2). A second loss component arises from the zero suppression threshold at 5 ADC counts. Since contributions to cluster charge below this value are suppressed, and since the cluster charge distribution widens with drift length due to diffusion, this cut creates apparent charge losses of typically 5% per metre drift length. In case of truncated means, only the smaller charges are maintained and the apparent loss increases to about 7% per metre. The size of this effect depends on the position, in ADC counts, of the most probable energy loss which had to be placed, as already discussed in section 6.1, at only 60 ADC counts. Previous TPC applications in low track densities [21] could use sense wire readout for dE/dx measurement which allows independent optimization of tracking and energy loss measurement.

In Pb+Pb interactions the apparent charge loss increases as a function of track density to values in excess of 20% in some parts of the VTPCs. This has turned out to be a major limitation to dE/dx resolution since a proper correction becomes very difficult. Two further sources of fluctuation have been found for this track density effect. The first one is induced by the negative undershoot present in the electronics time response, resulting in an apparent base line shift as discussed in section 5.6.3. The second one, of equal importance but related to the short-term time behaviour, is due to small and fast changes of the sense wire potential thus coupling an inverted signal across an entire padrow. Both effects, as well as the before mentioned threshold effect, can be corrected for off-line such that the good dE/dx resolution can be maintained in Pb+Pb collisions (see Fig. 26a, b); active work on these corrections is still continuing.

7.3 Truncation and dE/dx Resolution

The distribution of total charge on a track is nearly Gaussian for tracks of several metre length. Nevertheless the corresponding dE/dx resolution can be improved by typically 20% of its value using a truncated mean method. The optimum truncation procedure has been studied using data and Monte Carlo methods. The best performance was found by keeping only the 50% smallest clusters for the determination of the mean energy loss. The resulting resolution can be parametrized as $38\%/\sqrt{N_c}$ where N_c is the total number of clusters on a track. A look at Fig. 19 which gives the number of tracks as function of N_c shows that one can expect a best resolution around 3% for the 30% longest tracks, a mean resolution of about 4% and still about 6% resolution for tracks only measured in one of the VTPCs alone. An interesting side-product of this study is the re-establishing of the well-known fact [39] that Neon has the same specific resolution as Argon, although it has only half the specific ionization. The Monte Carlo calculations [40] show that this is partially due to the fact that the ionization potential in Ne is higher, and partially due to a modification of the energy-dependence of knock-on electrons from E^{-2} in Ar to about $E^{-2.2}$ in Ne (see also [41]).

A scatter plot of truncated energy loss against momentum is shown in Fig. 25 for positive secondaries in p+p and p+Pb collisions. A projection around 10 GeV/c momentum (Fig. 26a, b) shows the good separation of electrons, pions and protons and the clear appearance of a kaon peak, which allows, with proper cuts, a highly enriched kaon sample to be obtained.

8 Time-of-Flight Systems

Since particle identification by energy loss measurement alone fails at minimum ionization, and since –even with the good dE/dx resolution achieved– kaon selection on a track-by-track basis is not feasible, independent particle identifiers based on time-of-flight methods were foreseen in the NA49 detector concept. These systems have to comply with the following constraints (see also Fig. 1):

- installation possible only behind the MTPC or in a small zone between the two vertex magnets
- flight path about 14 m or 4 m respectively
- particle momentum at central rapidity 6 GeV/c for kaons and 10 GeV/c for protons
- necessary time resolution (rms) better than 100 ps
- high segmentation due to very high track densities in Pb+Pb events

Three different TOF systems were designed accordingly and installed as shown in Fig. 1:

1. a pixel scintillator system of 1800 elements behind the MTPCs, operating in the momentum range 3 to 12 GeV/c
2. a grid scintillator system of 200 elements positioned at larger angles behind the MTPCs, with momentum range 2 to 6 GeV/c
3. a system of PesTOF counters between the two vertex magnets for detection of particles at low rapidity with momenta up to 2 GeV/c.

In central Pb+Pb collisions about 7% of all tracked particles can be detected by these arrays.

8.1 Pixel Scintillator System

Two walls (TOF-TL and TOF-TR in Fig. 1) of 4.4 m^2 total surface contain 1782 individual scintillation detectors with rectangular scintillators glued directly to one photomultiplier per detector. The scintillators [42] have a thickness of 23 mm matched to the photocathode diameter, a height of 34 mm and horizontal widths between 60 and 80 mm, adjusted according to the local track density in Pb+Pb events. The photomultiplier [43] outputs are split and fed into constant-fraction discriminators followed by time-to-digital converters, and to charge-to-digital converters. This electronics system is housed in FASTBUS and VME crates.

After extrapolation of the tracks reconstructed in the MTPCs into the area of the TOF detectors, detailed corrections depending on charge deposition and relative position of the incident particle in each scintillator are performed.

The overall time resolution of the TOF-TR system is demonstrated in Fig. 27 where, for about 2 million tracks in 40000 central Pb+Pb events, the distribution of differences between the measured time-of-flight and that predicted from the measured momentum assuming the pion mass is shown. The distribution can be described by a Gaussian with a standard deviation of 60 ps. This value for the time resolution includes all contributions to the TOF measurement (start detector, uncertainties in tracking, etc.). The tail on the right side of the peak is due to pair creation by event-correlated γ's in the scintillators; slower kaons and protons are suppressed by a suitable dE/dx window.

Double hits due to the finite granularity, edge effects and background from γ's are the main sources of efficiency reduction. The sum of all losses, as determined experimentally by comparison with the TPC track data, amounts to 29% on average, with a maximum of 34% in the central region closest to the Pb–beam.

8.2 Grid Scintillator System

Two scintillator walls of 1.24 m^2 total surface (TOF-GL and TOF-GR in Fig. 1) comprise 186 individual scintillation detectors. Both walls are made up of a horizontal and vertical plane

of scintillator rods [44], each of them being viewed by 2 photomultipliers [45] at both ends. The rods have a length of 480 mm (horizontal) and 1300 mm (vertical) with a thickness of 24 (15) mm and a width of 25 (10) mm. Even in Pb+Pb collisions this arrangement with large surface scintillators is suitable because of the strong decrease of particle density at their position relative to the beam and due to the good inherent double-hit resolving capability profiting from the two-dimensional readout with its high granularity of 25×10 mm^2. The loss due to unresolved double hits is 13%; the total system efficiency has been estimated to be about 80%.

The electronics system of constant fraction discrimination, time-to-digital and charge-to-digital conversion is similar to the one used in the pixel system. The readout is done by a FIC VME/VSB processor transferring the data through a VSB-bus to the central DAQ.

For continuous control of operation laser signals are distributed among the scintillator rods through optical dividers and light fibres.

The four photomultiplier signals available per particle yield horizontal and vertical mean times which are approximately independent of hit position. Timing corrections due to position-dependent light collection times and due to amplitude dependences in the grid and start counters have to be applied. After correction, the overall time resolution has been determined to be 85 ps.

8.3 PesTOF Counter System

This system is a recent addition to the NA49 set-up introduced to improve identification in the backward hemisphere for particles below 2 GeV/c momentum. A first small array of 480×300 mm^2 surface has been operated in a position between the two vertex magnets (see Fig. 1). It is planned to extend this installation to a surface of about 1 m^2, installed on both sides of the beam.

PesTOF detectors [46] are small-gap (100 μm) spark counters operated in a four component gas mixture of Ar/Isobutane/Ethylene/Butadiene (76.9/20/2.5/0.6) at 12 bar. The inherent time resolution, depending on operation conditions, can reach values below 50 ps. Strips placed on the back of the semiconductive anode plane are read out on both sides by independent electronics, allowing for two-dimensional coordinate measurement with a resolution of a few mm in the strip direction and of order 1 mm in the direction orthogonal to the strips.

It has been shown that the expected space and multi-hit resolution can be reached. The performance in terms of time resolution is still being studied.

8.4 Combined dE/dx – TOF Performance

For particles in the acceptance of the TOF detectors dE/dx information from the TPCs is available simultaneously with the time of flight. The combination of both methods improves particle identification considerably. This is demonstrated by Fig. 28, where particles in the momentum range 5–6 GeV/c are sorted corresponding to their dE/dx signal and the mass (squared) obtained from the time-of-flight and momentum measurement.

At momenta above approximately 4 GeV/c the separation of the lighter particles (e, π) from the group of heavier ones (K, p, d) is performed essentially by dE/dx (see also Fig. 25), whereas the TOF measurement is needed for the distinction between kaons, protons and deuterons. Quantitatively, at 6 GeV/c –a momentum typical for midrapidity kaons– one obtains a 4 σ separation of pions and kaons (3 σ of it by dE/dx alone) and a 6 σ separation of kaons and protons (nearly exclusively by TOF).

9 Ring Calorimeter

The last element in the detection of secondary particles in NA49 is the Ring Calorimeter (RCAL in Fig. 1) placed 18 m downstream of the interaction target. Originally constructed for

the NA5 SPS experiment [6], it is used to measure neutral particle production in the projectile hemisphere in p+p and p+nucleus interactions. In Pb+Pb collisions, it gives information on transverse energy production rates [7] and event anisotropy [47].

The calorimeter has a lead/scintillator sandwich front section of 16 radiation lengths backed by an iron/scintillator sandwich section of 6 interaction lengths. It is cylinder shaped with an inner bore of 56 cm diameter and an outer radius of 151 cm. The sensitive area is subdivided into 240 cells, configured in 10 radial rings and 24 azimuthal sectors, read out by photomultipliers via wavelength shifter bars. The energy resolution can be parametrized by $\sigma(E)/E = 1.2/\sqrt{E(\mathrm{GeV})}$. As the distance from target is substantially larger than in the original NA5 experiment, the calorimeter is sensitive only in the forward hemisphere between rapidities of about 3 and 5 unless used with a target configuration down-stream of the magnets.

10 Conclusions

The NA49 large acceptance spectrometer has been in full operation since fall 1995, after a construction period of only three years. In the initial phase of exploitation, it has been shown that the ambitious detector programme of precision tracking and identification of up to more than 1000 particles per event in central Pb+Pb interactions could be successfully achieved. The first two years of operation have been dedicated to central Pb+Pb interactions, where 1.5 million events were recorded in about 6 weeks under optimum running conditions.

In additional data taking periods using proton and pion beams with the same detector set-up the physics programme was extended to hadron+proton and hadron+nucleus collision studies, thus covering all hadronic initial states available at the CERN SPS (see [48]). The operation of the detector has been stable and reliable throughout.

Given the complexity of both the experimental environment and of the tracking and particle identification equipment, it is not surprising that the detailed study and optimization of detector response and reconstruction software is still progressing. Special attention has been given to the limiting performance in the regions of very high particle densities encountered in central heavy ion reactions. As described in this paper such limits become visible, in particular in comparison with the less critical p+p and p+Pb collisions, in detector operation as well as in the performance of tracking and particle identification.

Acknowledgements

It is a pleasure to thank the operating crews of the CERN SPS accelerator and beamlines who made this experimental programme possible. We gratefully acknowledge the work of many groups at CERN (EP/EC, EP/ISS, EP/TA1, EST/SM, EST/SU, LHC/ECR, SL/EA, ST/HM) and at the collaborating institutes who participated in the construction and installation of the experiment and assure its operation.

This work was supported by the US Department of Energy (contract DE-ACO3-76SFOOO98), the US National Science Foundation, the Bundesministerium für Bildung und Forschung, Germany, the Alexander von Humboldt Foundation, the UK Engineering and Physical Sciences Research Council, the Polish State Committee for Scientific Research (2P03B 01912 and 2P03B 9913), the Hungarian Scientific Research Foundation (contracts T22339, T7330 and OAB-94/0197), the EC Marie Curie Foundation, and the Polish-German Foundation.

References

[1] CPS Magnet Handbook (1976)
[2] J. Harris et al., Nucl. Instr. and Meth. **A315** (1992) 33
[3] G. Rai et al., IEEE Trans. Nucl. Sci. **37** (1990) 56
[4] F. Bergsma CERN, private communication
[5] C. Blyth, B. Lasiuk, H. Ströbele, S. Trentalange and C. Whitten, *The NA49 Magnet Mapping Programme*, Internal Report (1995)
[6] C. DeMarzo et al., Nucl. Instr. and Meth. **217** (1983) 405
[7] T. Alber et al., Phys. Rev. Lett. **75** (1995) 3814
[8] I. Otterlund et al., Nucl. Phys. **B198** (1987) 407,
A. Ferrari et al., Z. Phys. **C71** (1996) 75
[9] RD 32 Final Report, CERN LHCC 96-16
[10] T. Alber et al., Nucl. Instr. and Meth. **A349** (1994) 56
[11] HITEC, Bronkhorst, Ruurlo/NL
[12] Orbisphere Laboratories, Neuchatel/CH
[13] Endress+Hauser Messtechnik GmbH+Co, Maulburg/D
[14] A. Cattai et al., Internal Report DELPHI 89-63
[15] S. Wenig, Nucl. Instr. and Meth. **A409** (1998) 100
[16] FRIATEC, Mannheim/D
[17] A. Kühmichel, Nucl. Instr. and Meth. **A360** (1995) 52
[18] Araldite 2011, CIBA, Basel/CH
[19] RTV 3145, Dow Corning, Wiesbaden/D
[20] H.G. Fischer, CERN (unpublished)
[21] W. Blum and L. Rolandi, *Particle Detection with Drift Chambers*, Springer 1993
[22] Cicorel, CICOREL SA, Crissier/CH
[23] S.R. Klein et al., STAR Note 239, BNL, Brookhaven, NY (1995)
[24] F. Bieser et al., Nucl. Instr. and Meth. **A385** (1997) 535
[25] Orbit Semiconductor, Sunnyvale/CA (USA)
[26] S.A. Kleinfelder, IEEE Trans. Nucl. Sci. **35** (1988) 1988 and **37** (1990) 1230
[27] M. Bosteels, WELDEC, October 4-7 1994, Lausanne/CH
[28] Signal Computing Limited (Model SRI356S), Guildford/UK
[29] W. Rauch et al., IEEE Trans. Nucl. Sci. **41** (1994) 30
[30] W. Blum et al., The ALEPH Handbook, ALEPH 89-77 CERN (1989),
D. Decamp et al., Nucl. Instr. and Meth. **A294** (1990) 121
[31] A. DeMin et al., IEEE Trans. Nucl. Sci. **42** (1995) 491
[32] Source produced at ISOLDE Isotope Separator, CERN
[33] Precision Survey provided by CERN EST/SU Group
[34] CARL ZEISS Jena Precision Automatic Level NI002A, Jena/D
[35] WILD automatic Nadir Instrument NL Leica, Heerbrugg/CH
[36] Spectron Laser Systems, Warwickshire/UK
[37] R. Gluckstern, Nucl. Instr. and Meth. **24** (1963) 381
[38] M. Fuchs, Nucl. Instr. and Meth. **A367** (1995) 394
[39] I. Lehraus et al., Nucl. Instr. and Meth. **196** (1982) 361,
I. Lehraus et al., Nucl. Instr. and Meth. **200** (1982) 199
[40] B. Lasiuk, Nucl. Instr. and Meth. **A409** (1998) 402
[41] H. Fischle et al., Nucl. Instr. and Meth. **A301** (1991) 202

[42] TOF-TR: Bicron BC-418, BICRON/USA
TOF-TL: similar scintillator produced at JINR Dubna/Russia
[43] TOF-TR: Philips XP-2972, Philips Photonics/F
TOF-TL: FEU-87, MELZ, Moscow/Russia
[44] Bicron BC-408, BICRON/USA
[45] Hamamatsu R-3478, Hamamatsu Photonics, Schüpfen/CH
[46] E. Badura et al., Nucl. Instr. and Meth. **A379** (1996) 468
[47] T. Wienold (for NA49 collaboration), Nucl. Phys. **A610** (1996) 76c
[48] CERN/SPSC 98–4 and CERN/SPSC 99–4

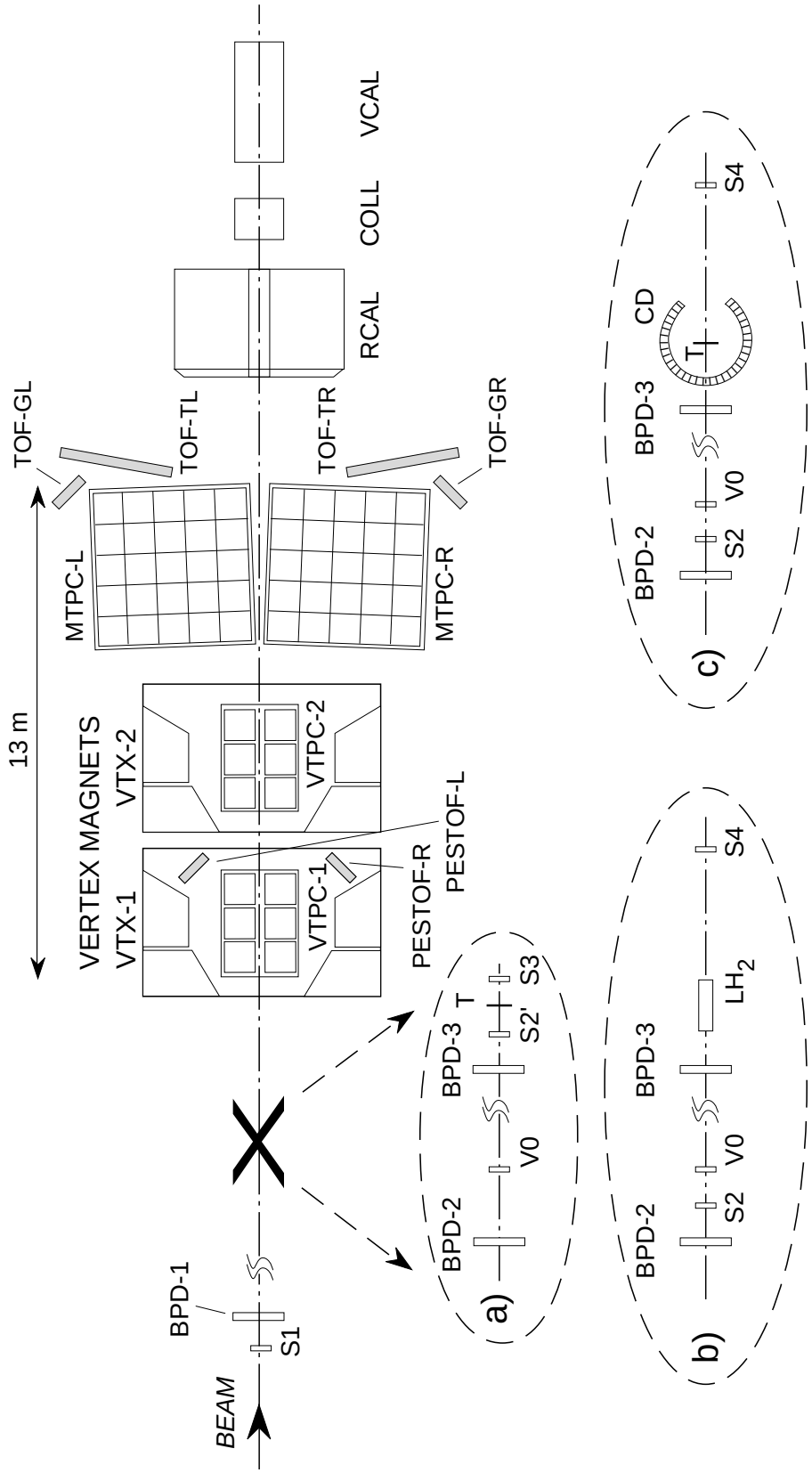

Figure 1: Set–up (not to scale) of NA49 experiment with different beam definitions and target arrangements for a) Pb+Pb, b) p+p and c) p+A collisions. The target position is at the front face of the first Vertex Magnet (VTX-1).

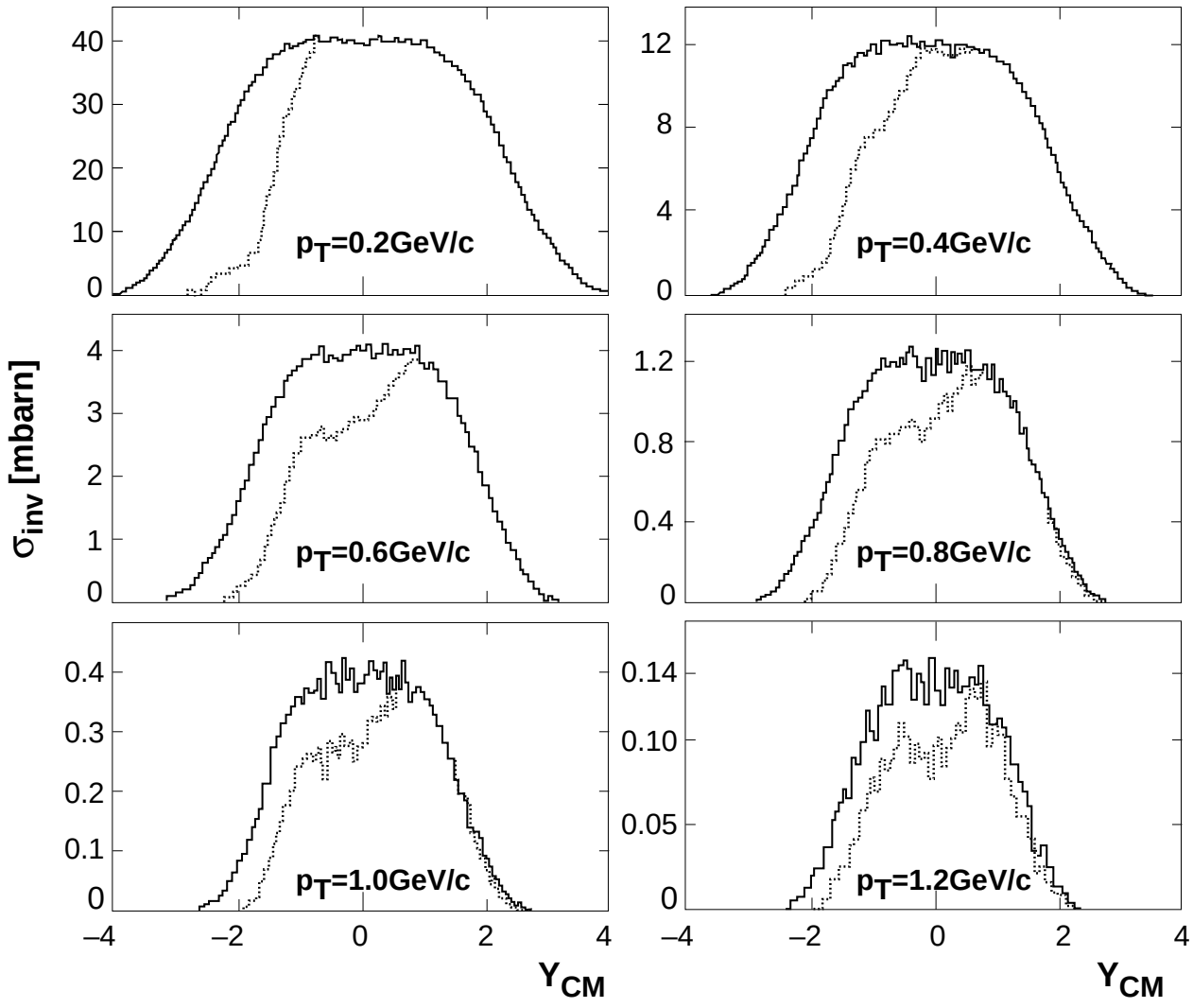

Figure 2: Rapidity distribution of negative pions produced in p+p collisions at 158 GeV/c for different bins in transverse momentum. The full line represents Monte-Carlo generated particles, the hatched line accepted particles.

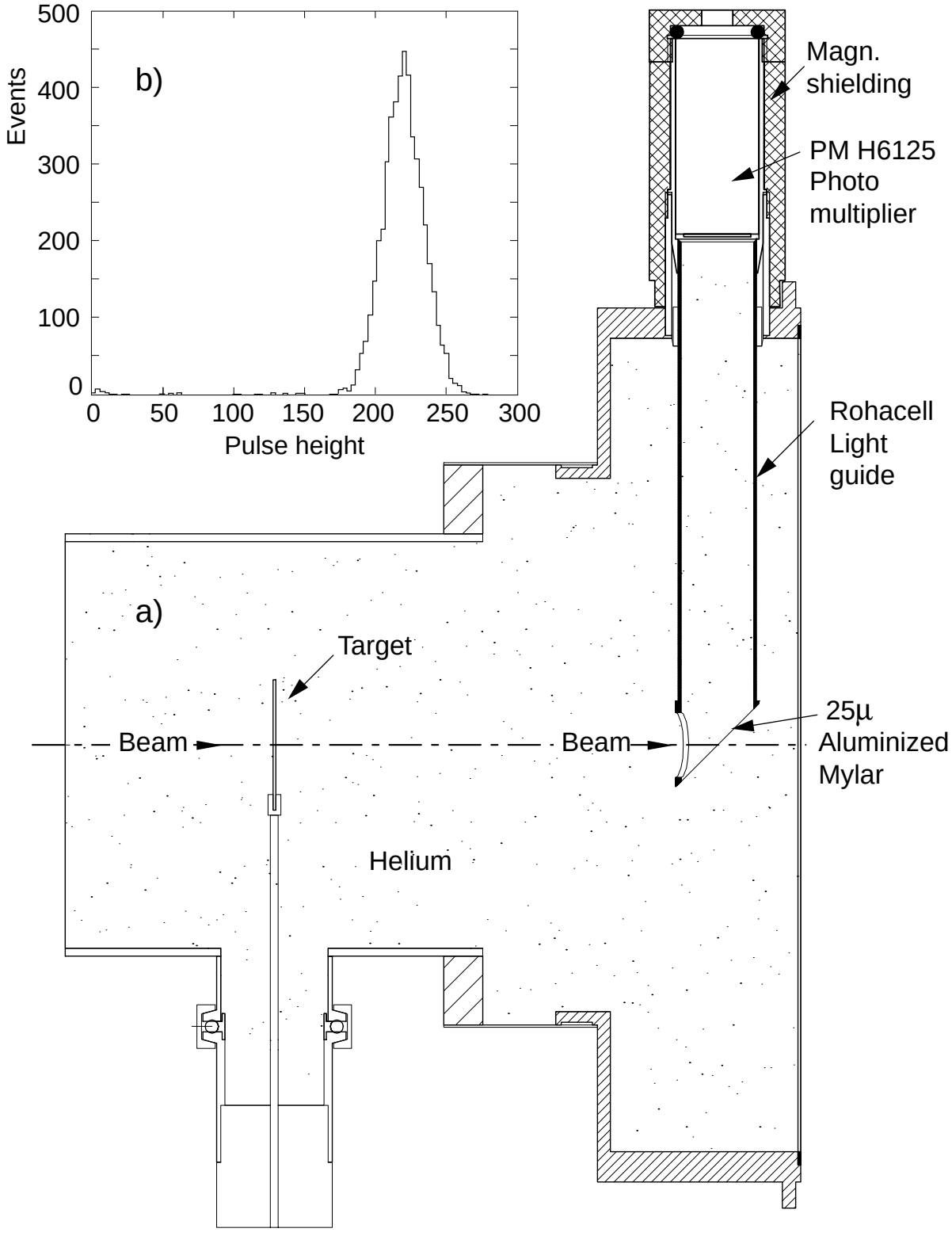

Figure 3: Helium Gas-Čerenkov counter for Pb-beam particles: a) schematic cross sectional view, b) amplitude spectrum.

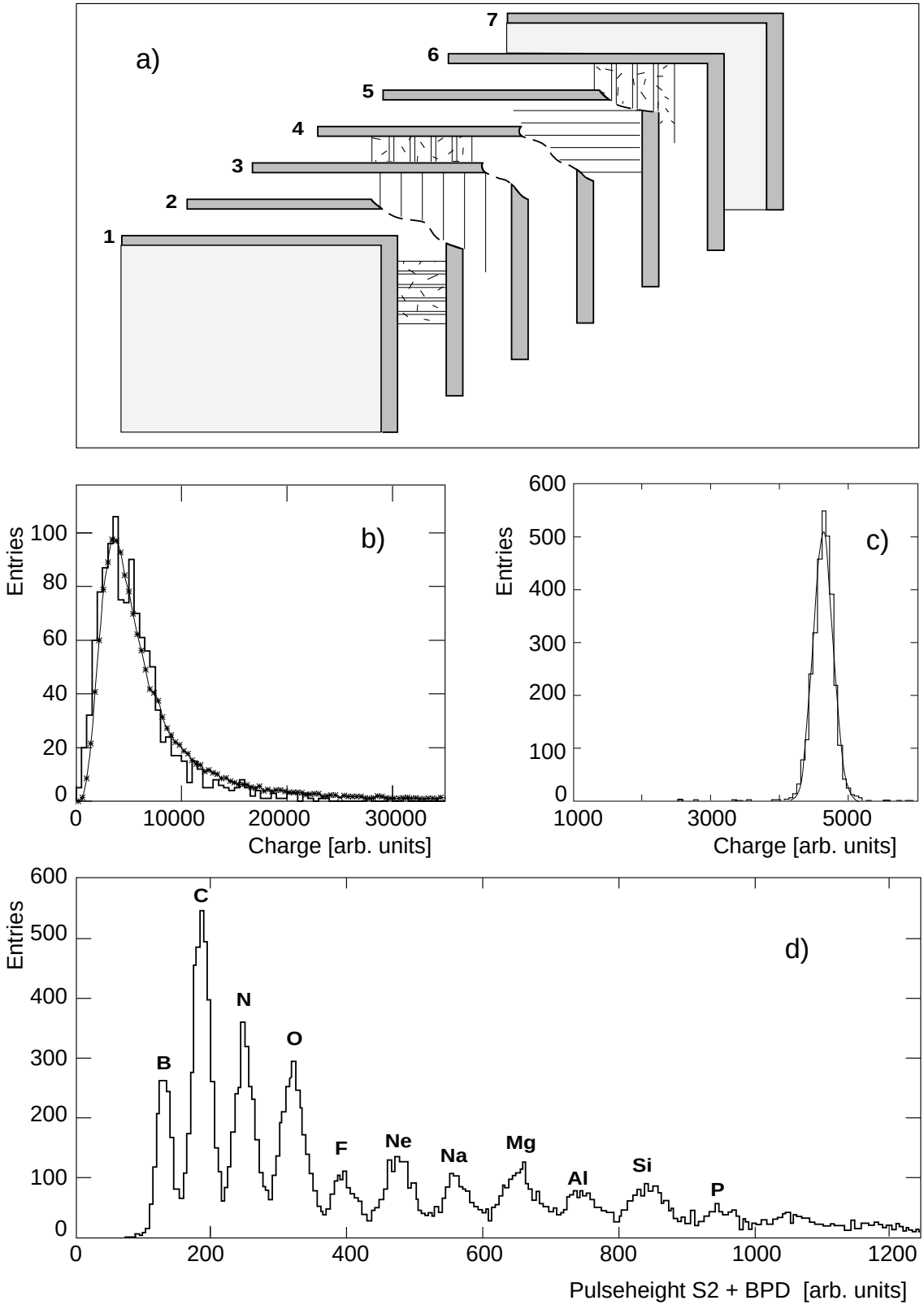

Figure 4: Beam position detectors: a) schematic view showing wire planes (3, 5), cathode read-out planes (2, 6), central plane (4) and closing windows (1, 7); b) and c) total charge distributions for proton– and Pb–beam particles, respectively; d) separation power for Pb–beam fragments by combining the charge sum signal of the 6 BPD planes with the information from the S2 scintillation counter.

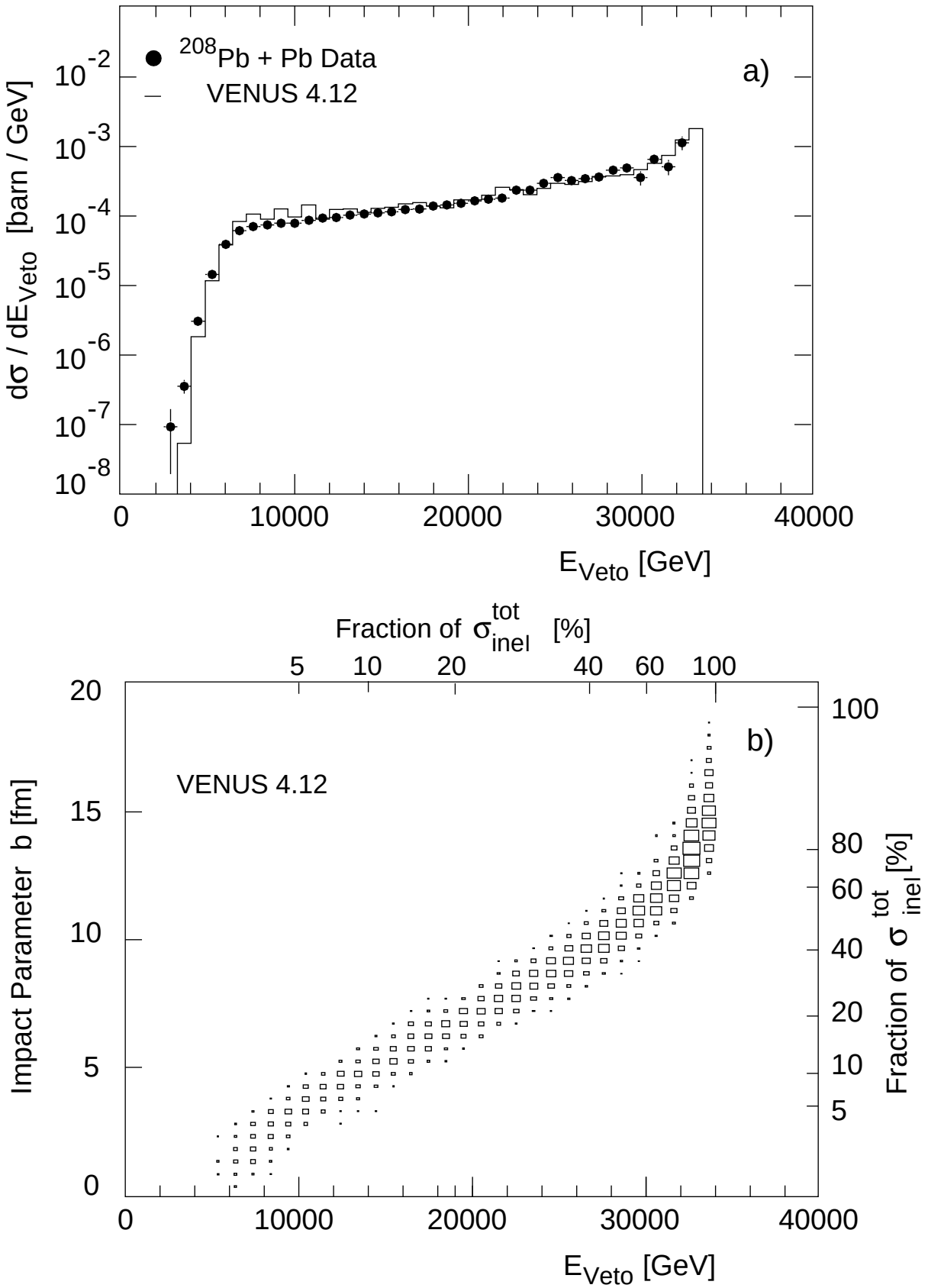

Figure 5: a) Energy spectrum of the Veto Calorimeter in Pb+Pb interactions; b) impact parameter and fraction of total inelastic cross section related to the energy in the Veto Calorimeter as derived from the VENUS model.

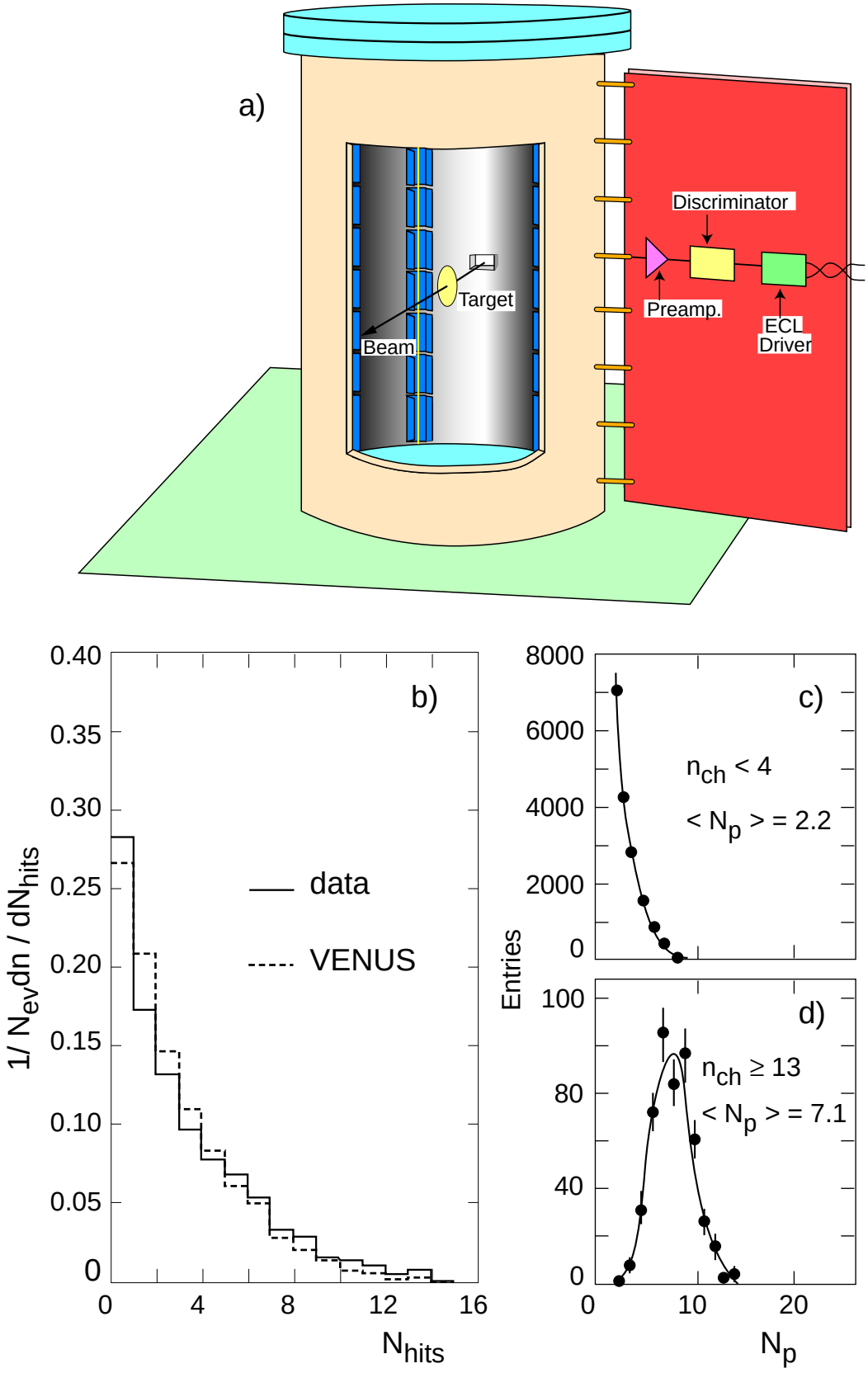

Figure 6: Centrality Detector: a) schematic view, b) distribution of recorded hits in p+Pb interactions, c) and d) distribution of number of participants N_p with n_{ch} hits in the CD-counter as derived from the VENUS model.

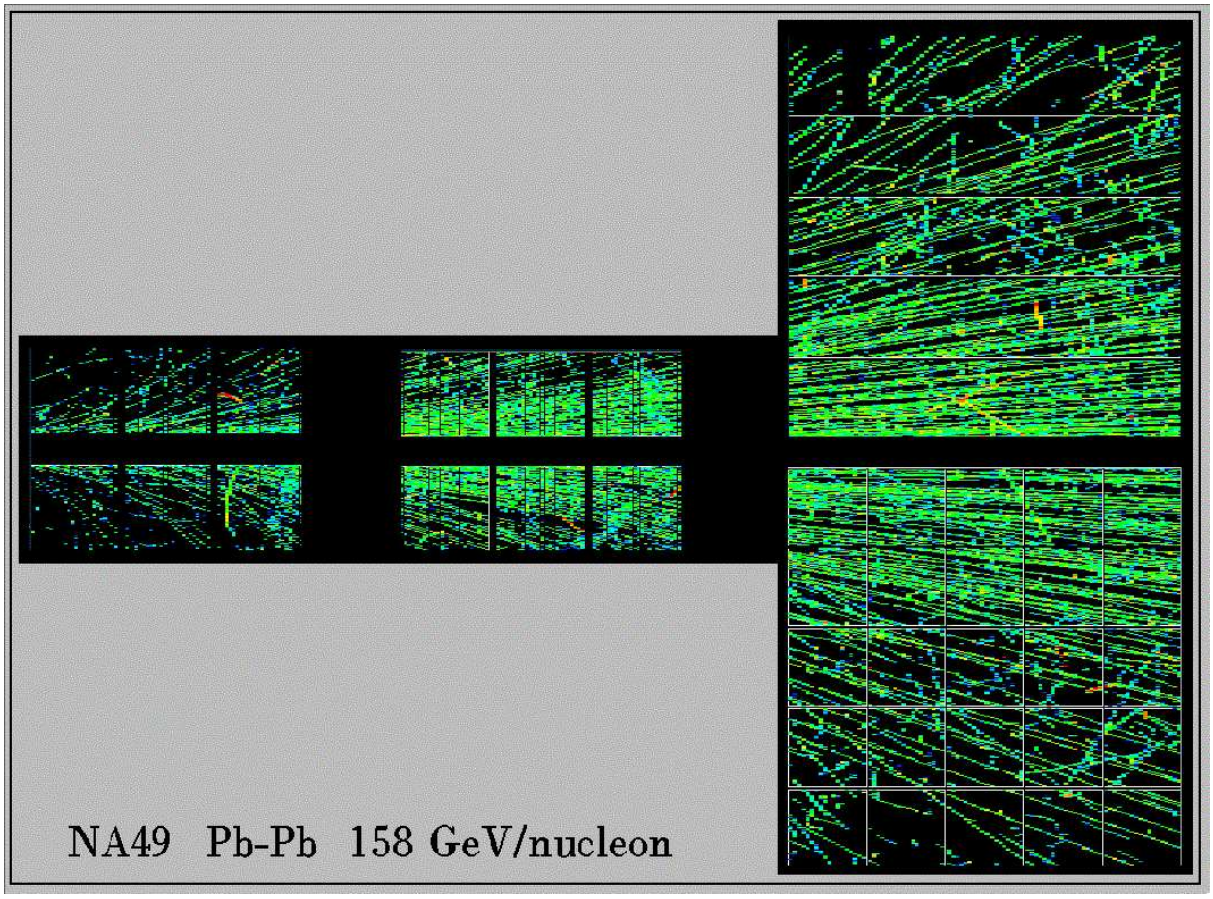

Figure 7: Topview of a central Pb+Pb event as detected by the four TPCs. Only a 7 mm high slice around the beam plane is depicted in order to allow for a resolution of tracks in the projection.

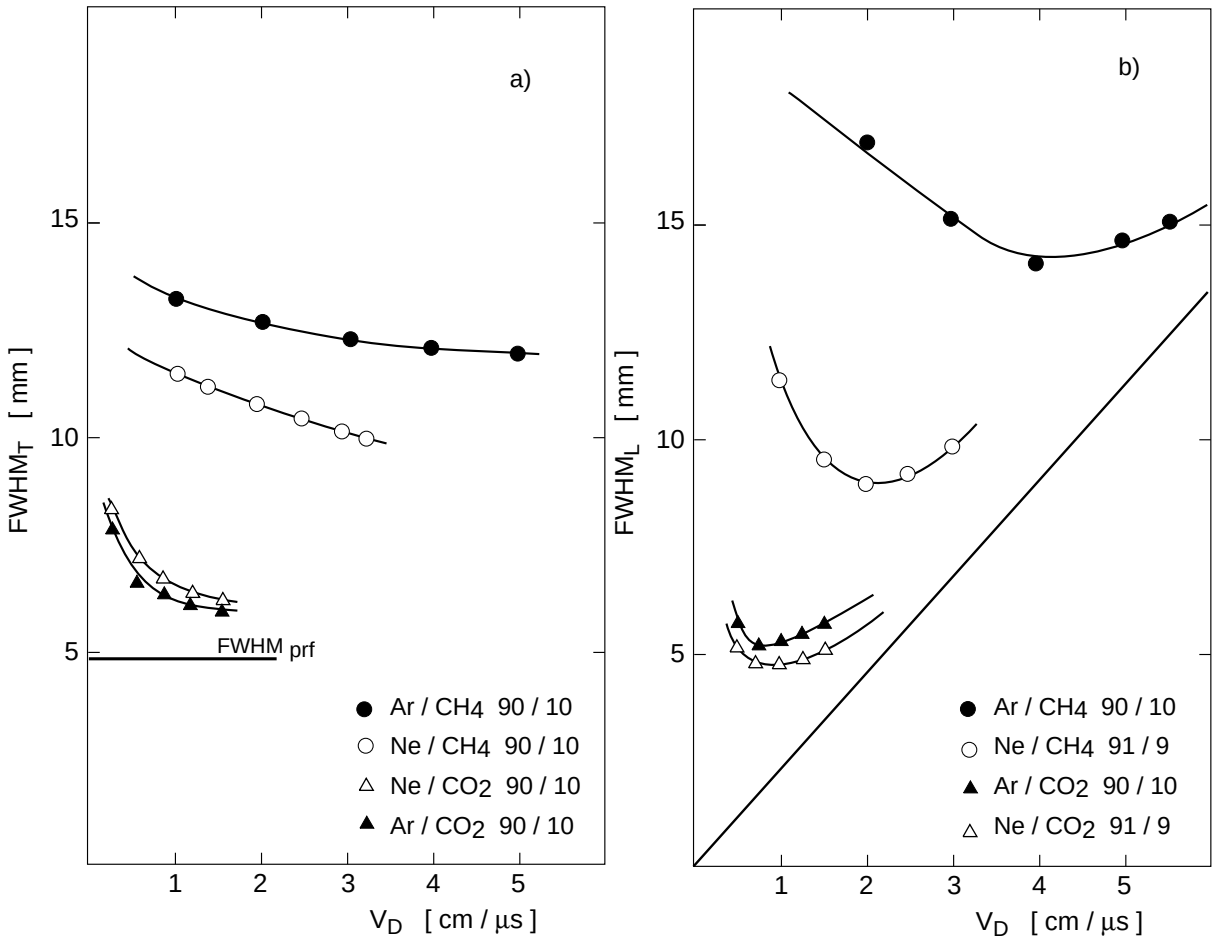

Figure 8: FWHM of charge distribution after 60 cm drift for different gas mixtures a) in transverse (bending plane) and b) in longitudinal (drift) direction. The limits given by the pad response function (prf) and the electronics shaping time, respectively, are indicated as straight lines.

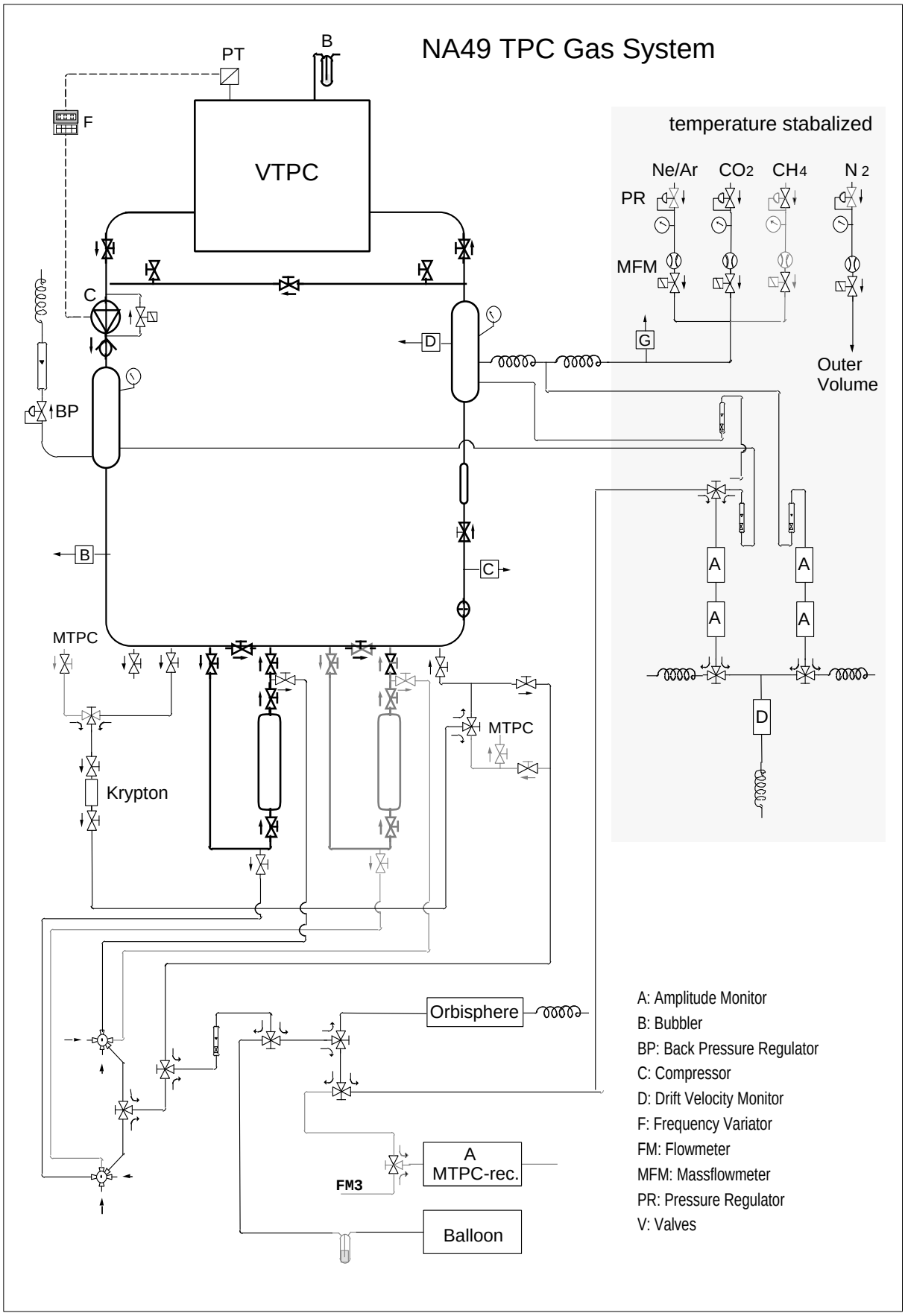

Figure 9: Layout of one of the four TPC gas recirculation systems.

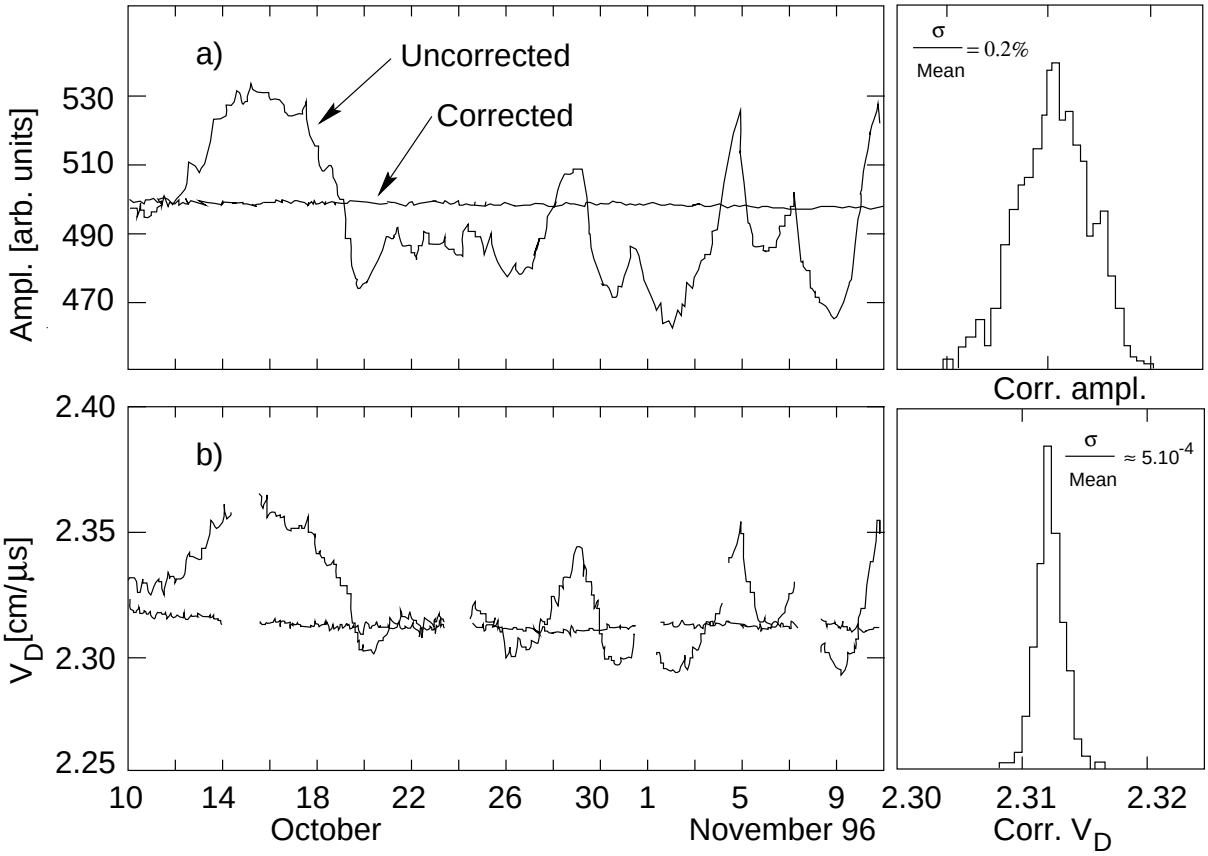

Figure 10: Uncorrected and corrected time dependence, and resolution of the gas monitor system: a) for amplitude b) for drift velocity counters.

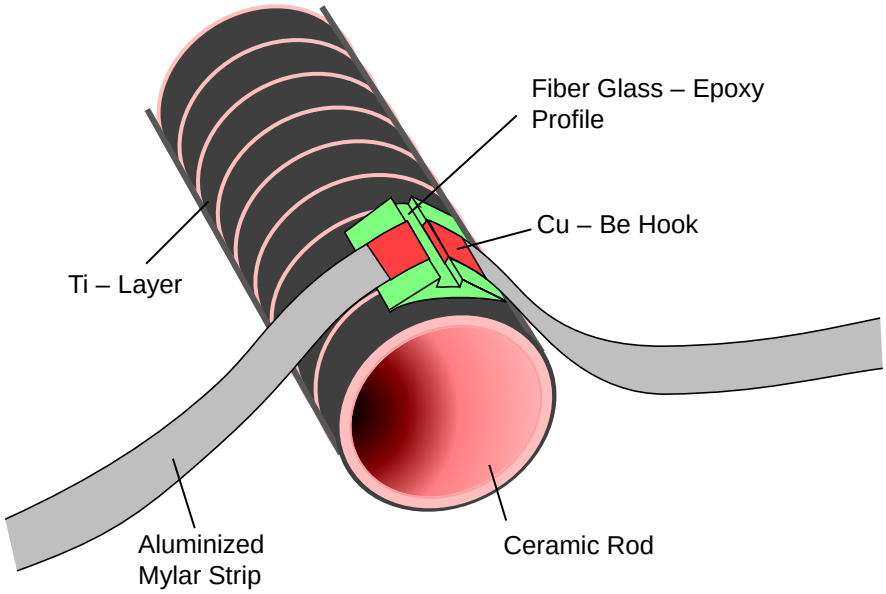

Figure 11: Fixation of field strips in TPC field cages.

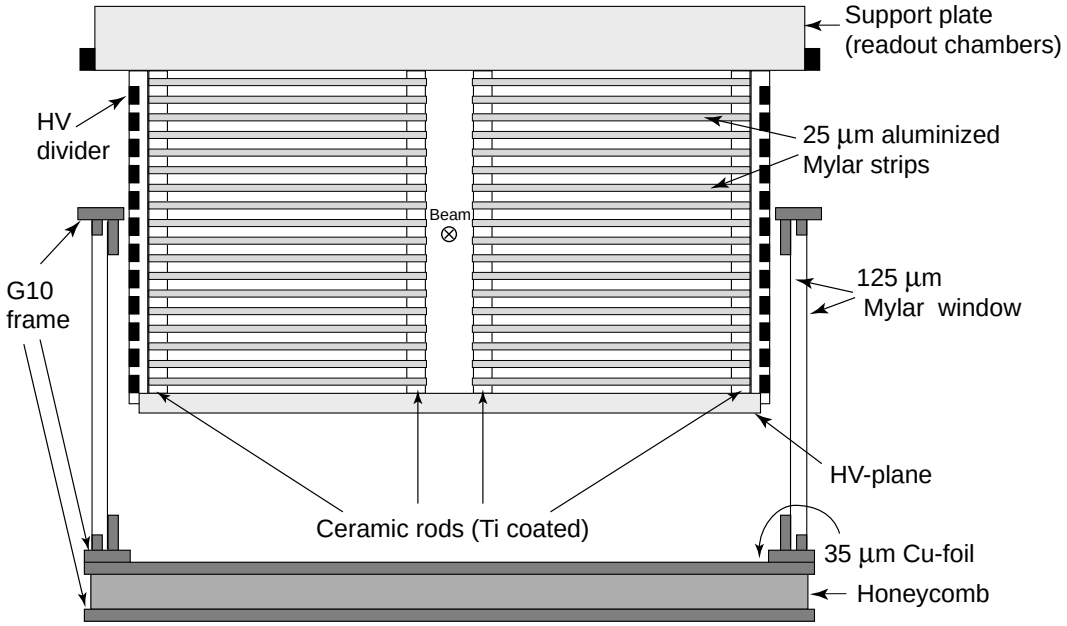

Figure 12: Schematic drawing of the assembly of one of the VTPCs showing the support plate housing the readout chambers, the two field cages on both sides of the beam, and the gas envelope.

Figure 13: View into the field cage of a MTPC.

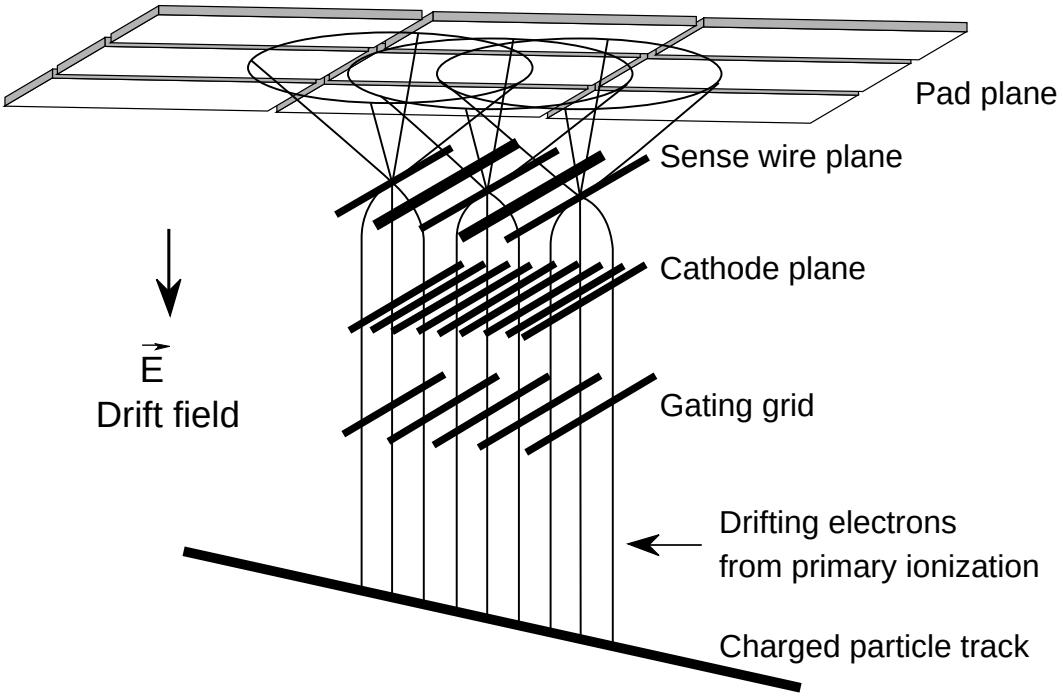

Figure 14: Schematic layout of the TPC readout chambers. Note that the drift is vertically upwards.

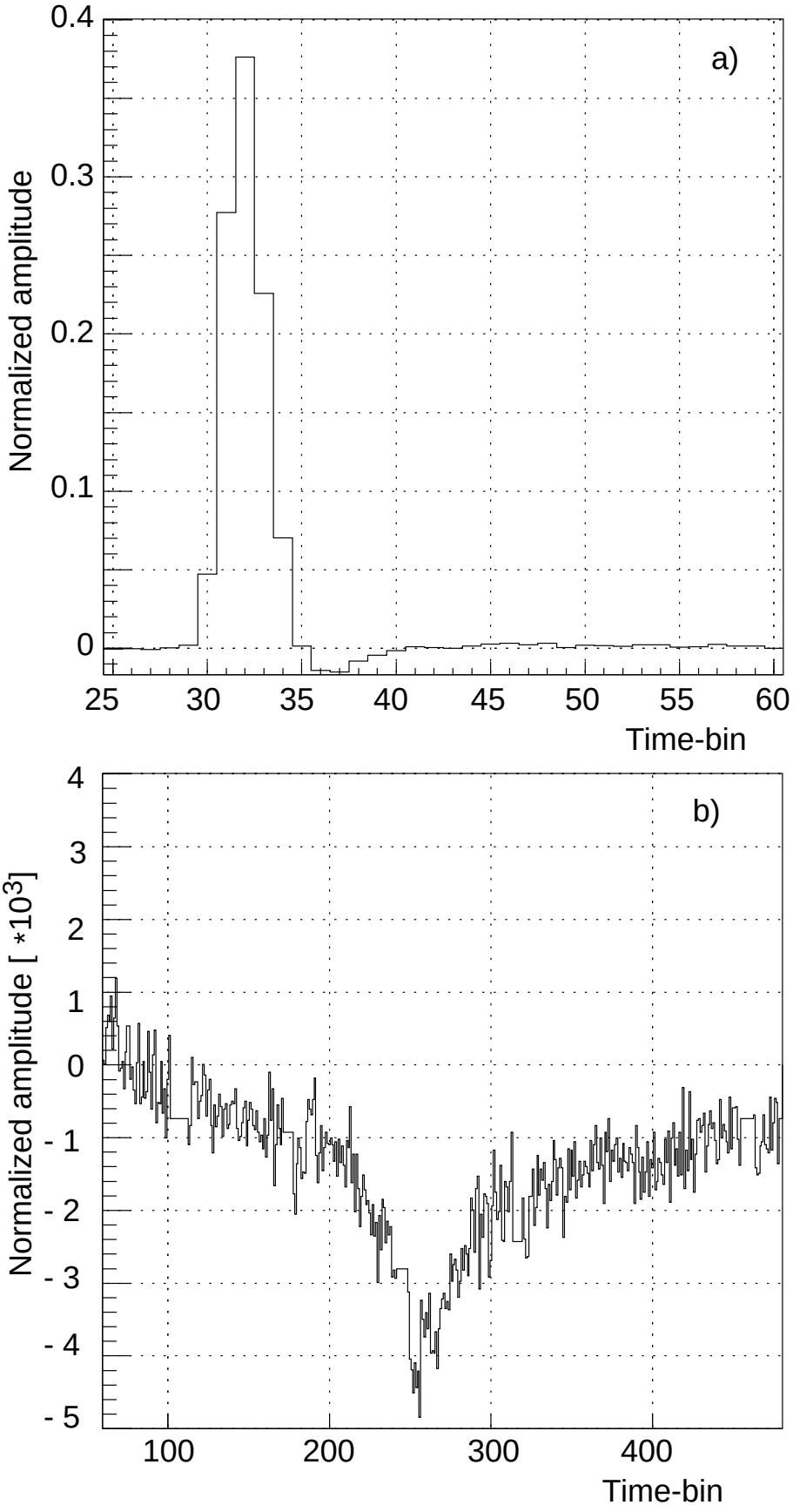

Figure 15: Time response of the NA49 electronics a) for times up to 3 μs b) for the complete drift time. A time bin corresponds to 100 ns.

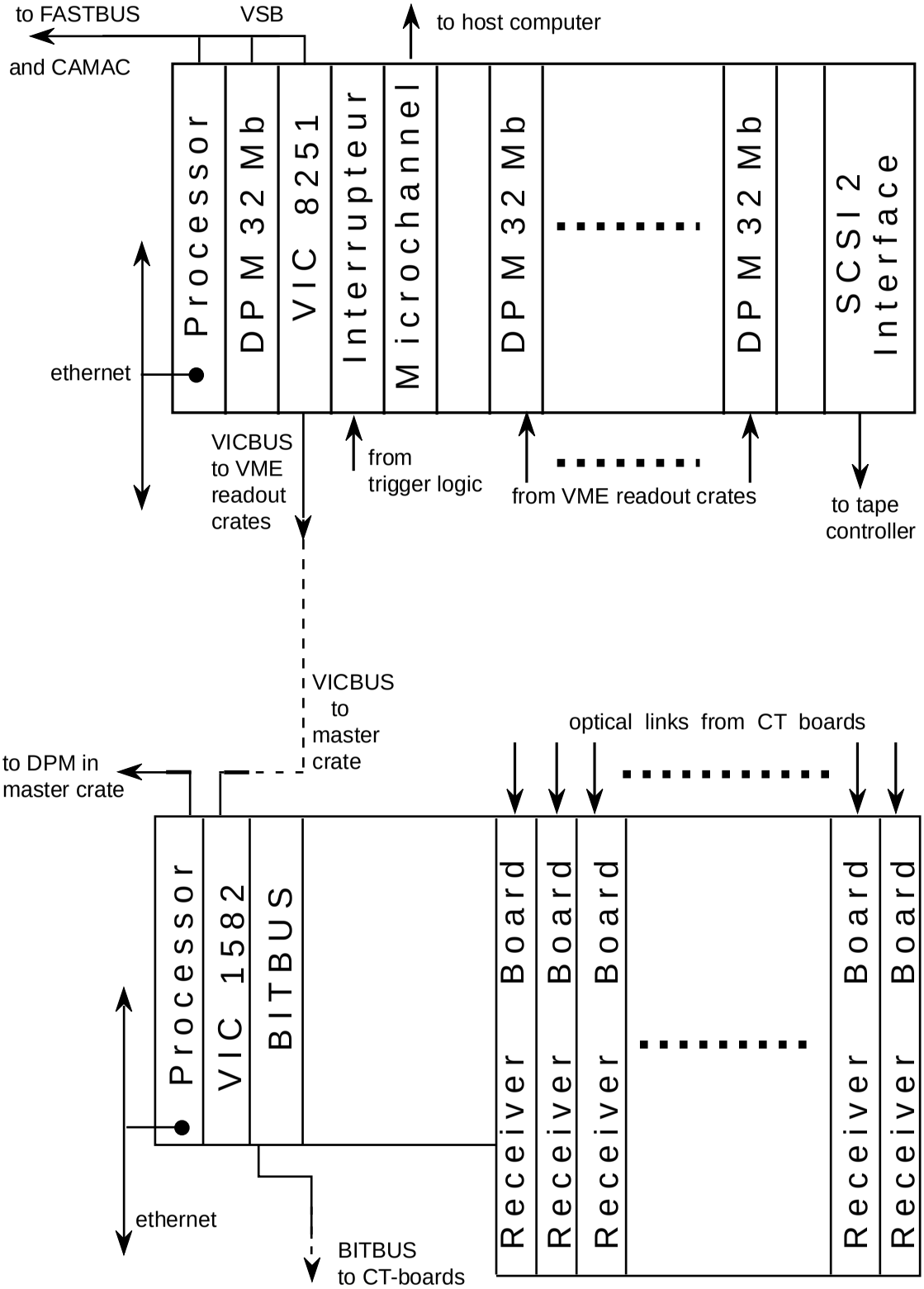

Figure 16: Schematic layout of the data acquisition system.

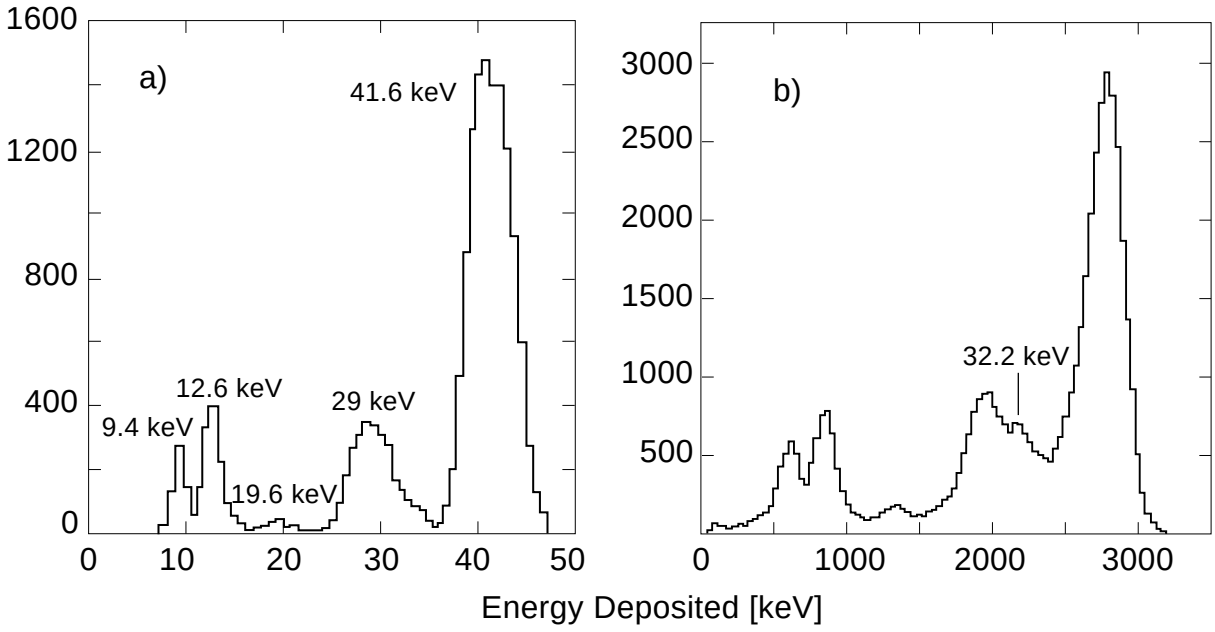

Figure 17: Charge spectrum from ^{83}Kr decay: a) Monte Carlo generated, b) real data from MTPC.

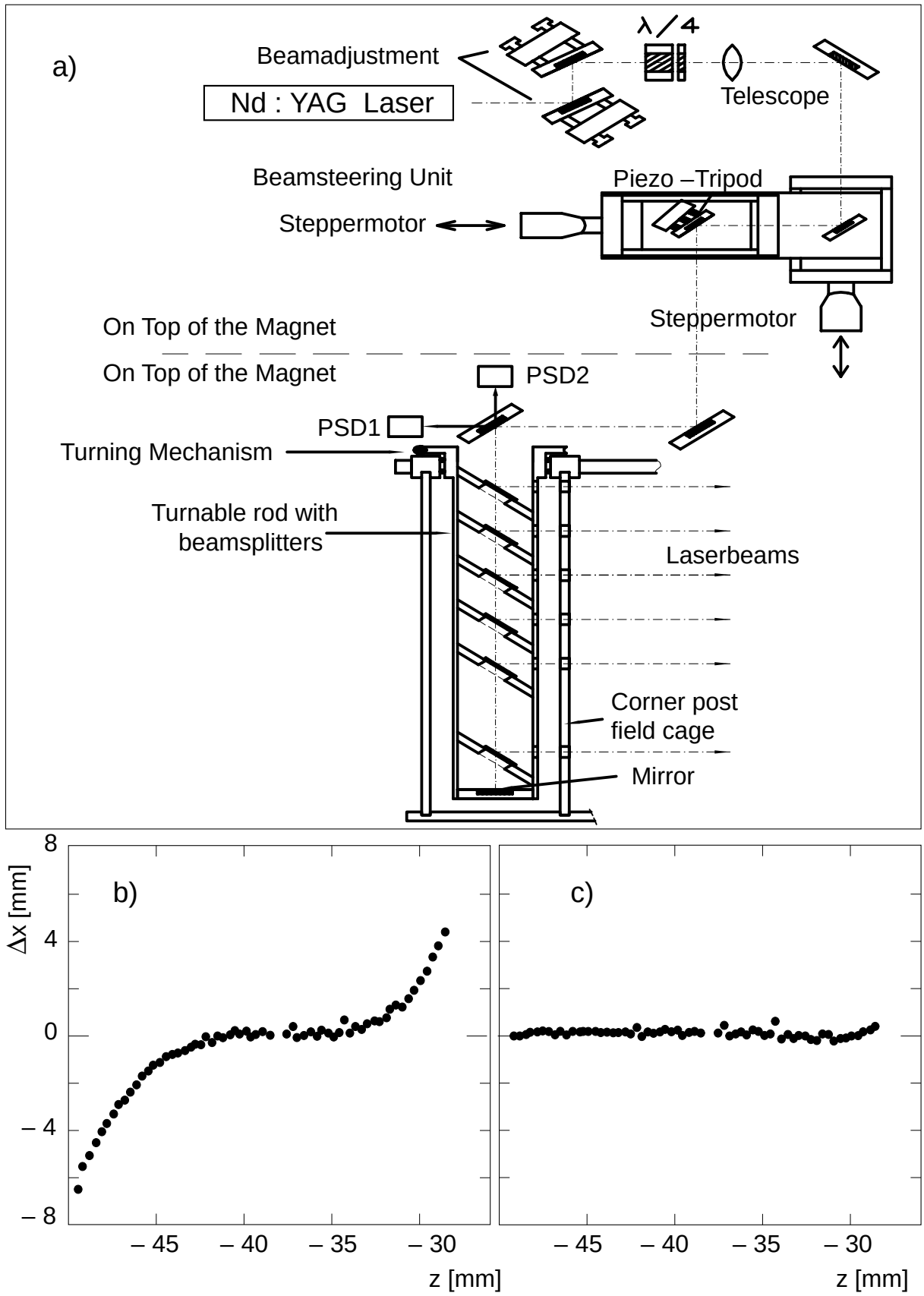

Figure 18: Laser system of one TPC: a) optical layout, b) and c) residual distribution in the bending plane with respect to a linear fit to laser tracks without and with $E \times B$ correction, respectively.

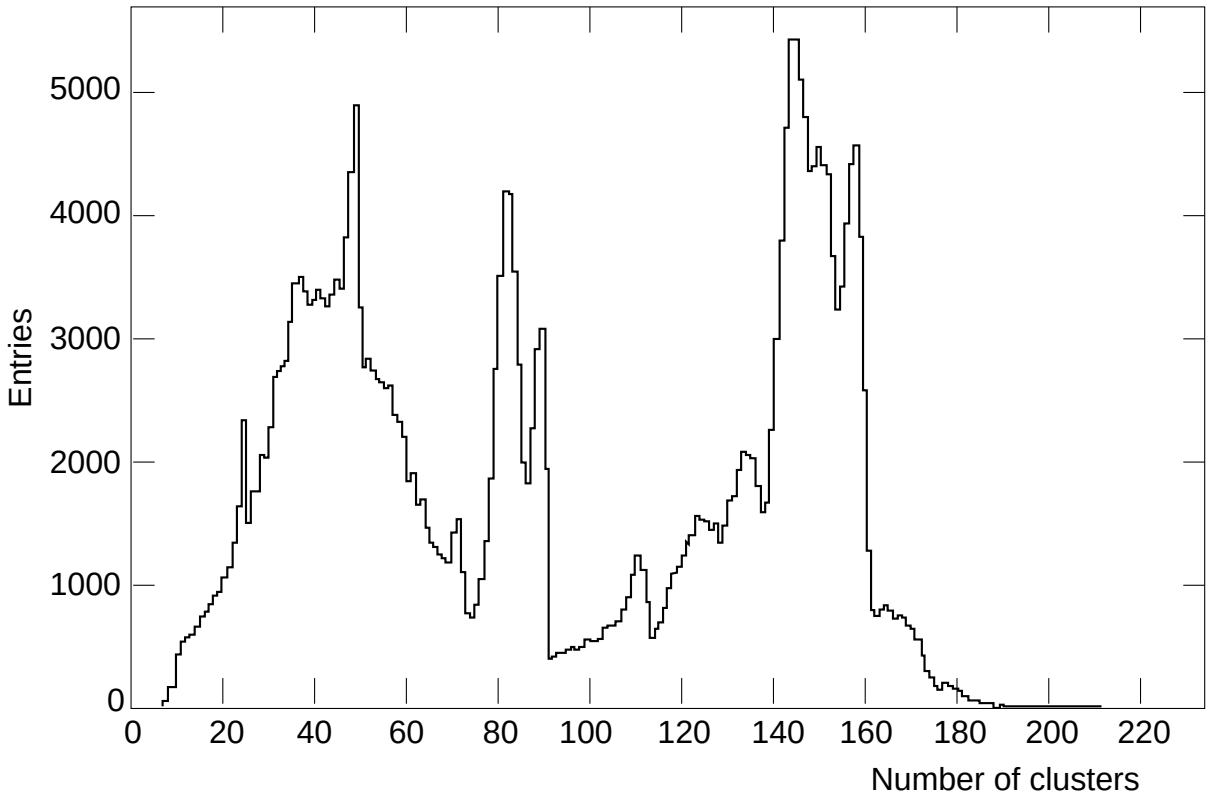

Figure 19: Distribution of total number of clusters per track.

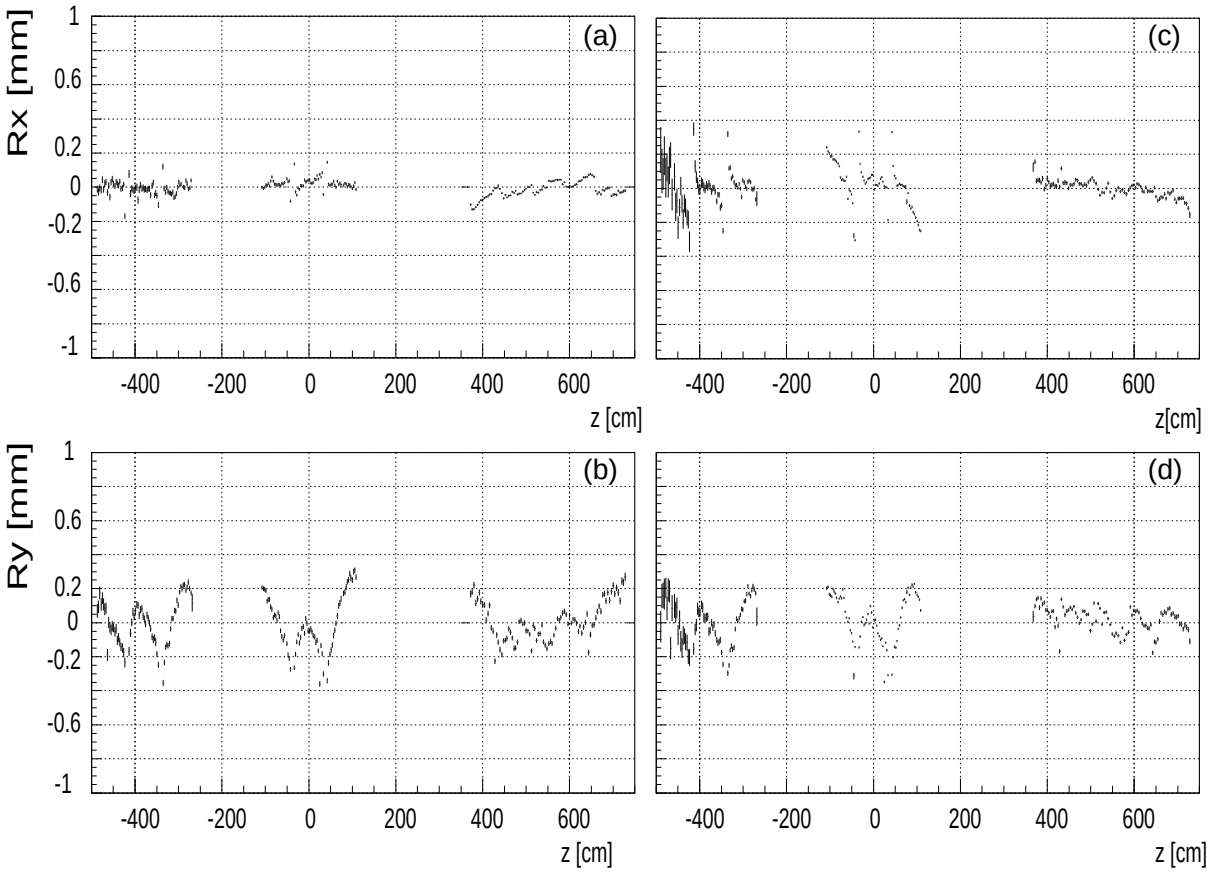

Figure 20: Average TPC residuals after correction for optical survey geometry: a) and b) represent residuals in horizontal (x) and vertical (y) coordinates without magnetic field, c) and d) with nominal magnetic field. Note z-direction is along the beam.

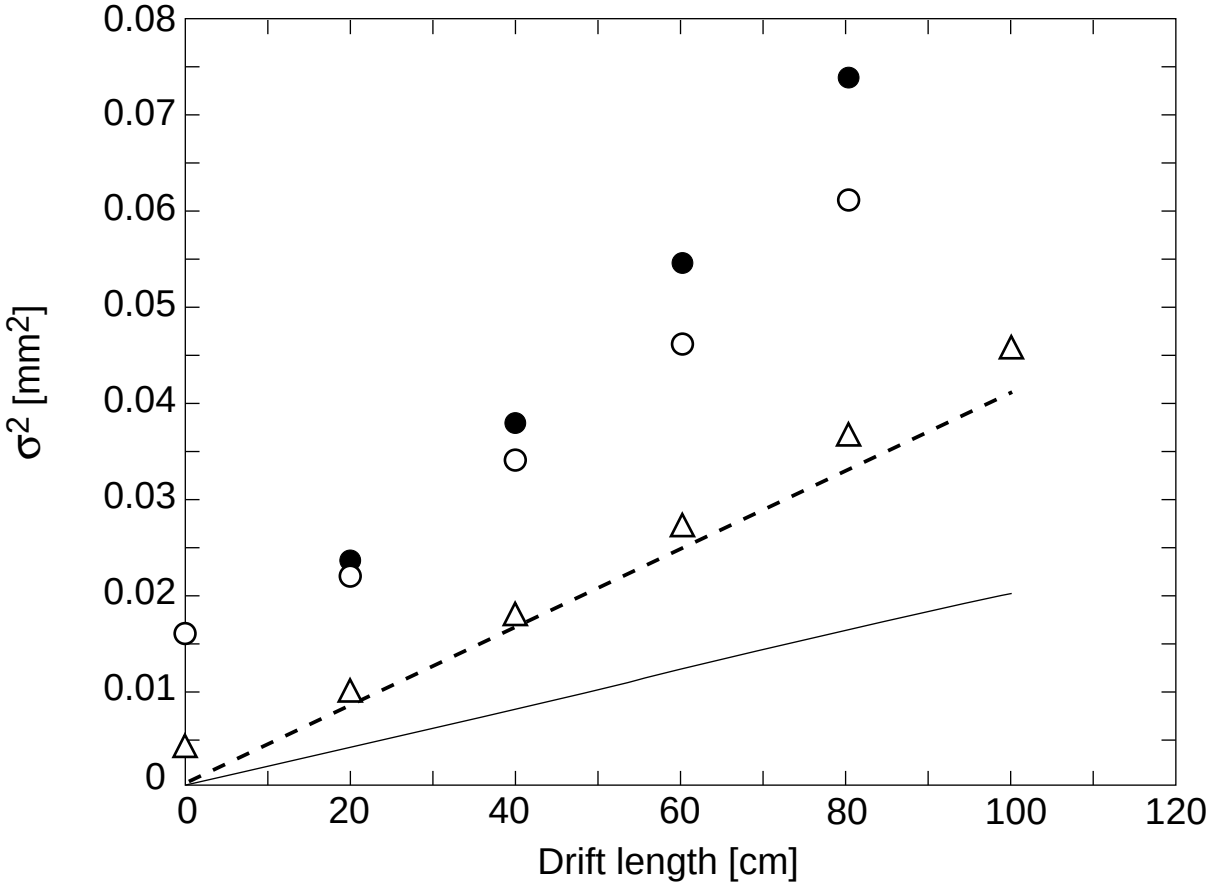

Figure 21: σ^2 of residual distribution in the bending plane from muon tracks in a MTPC as function of drift length. Full circles: measurement, full line: contribution of diffusion only, hatched line: contribution of diffusion multiplied by factor 2, open triangles: simulation containing diffusion and gas gain fluctuations, open circles: simulation including in addition all contributions to σ_0–term. For details see chapter 6.1.

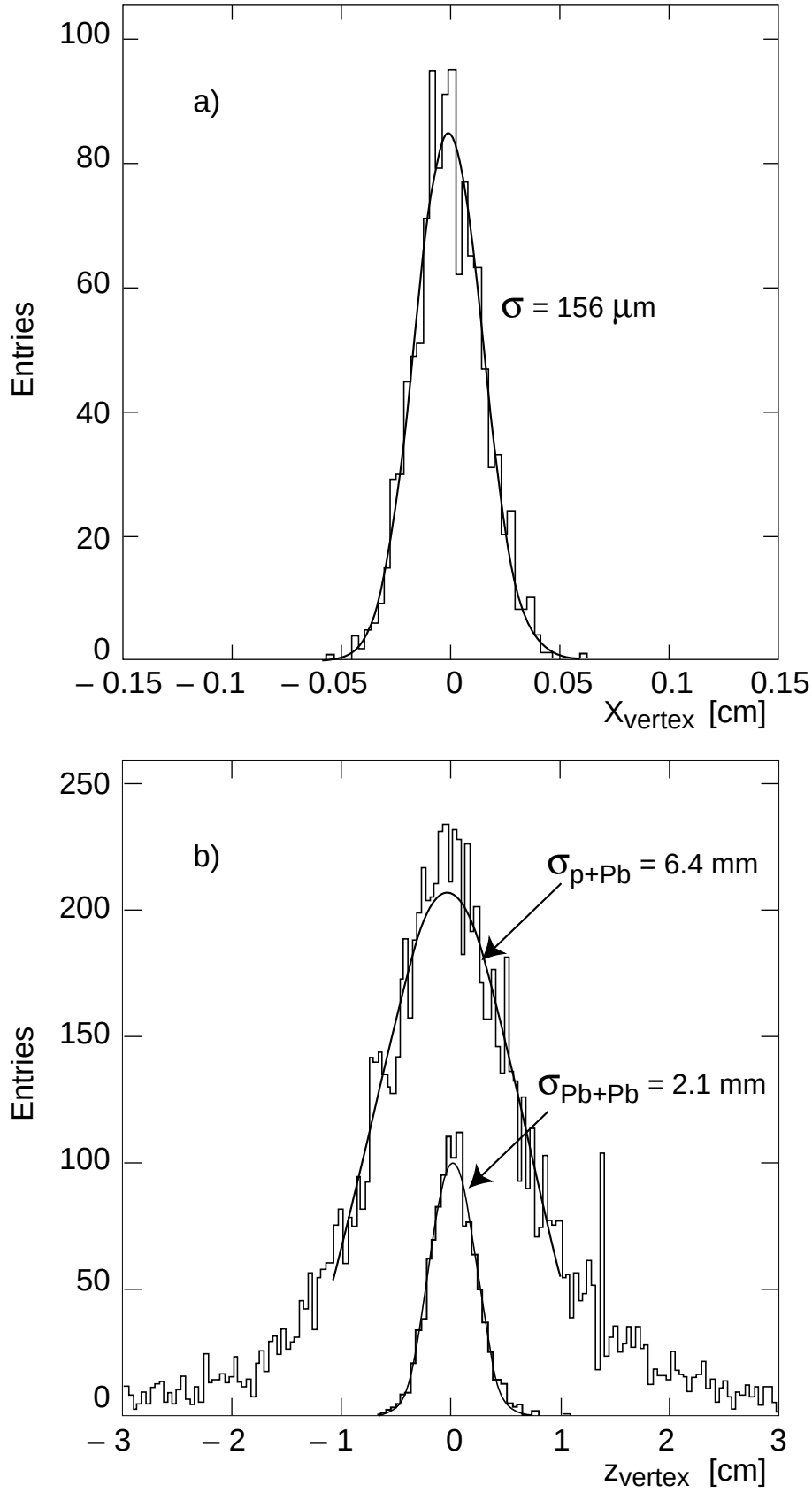

Figure 22: Distribution of vertex coordinates a) in the bending plane (x-coordinate) for central Pb+Pb events and b) along the beam direction (z-coordinate) for p+Pb and central Pb+Pb interactions.

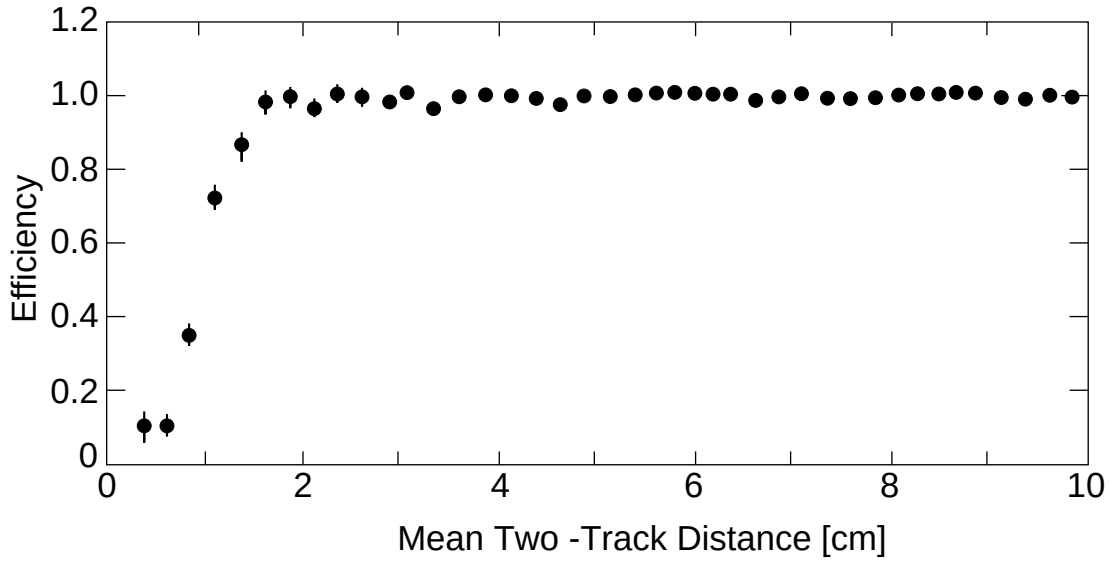

Figure 23: Two track resolution as determined from event mixing in VTPC-2.

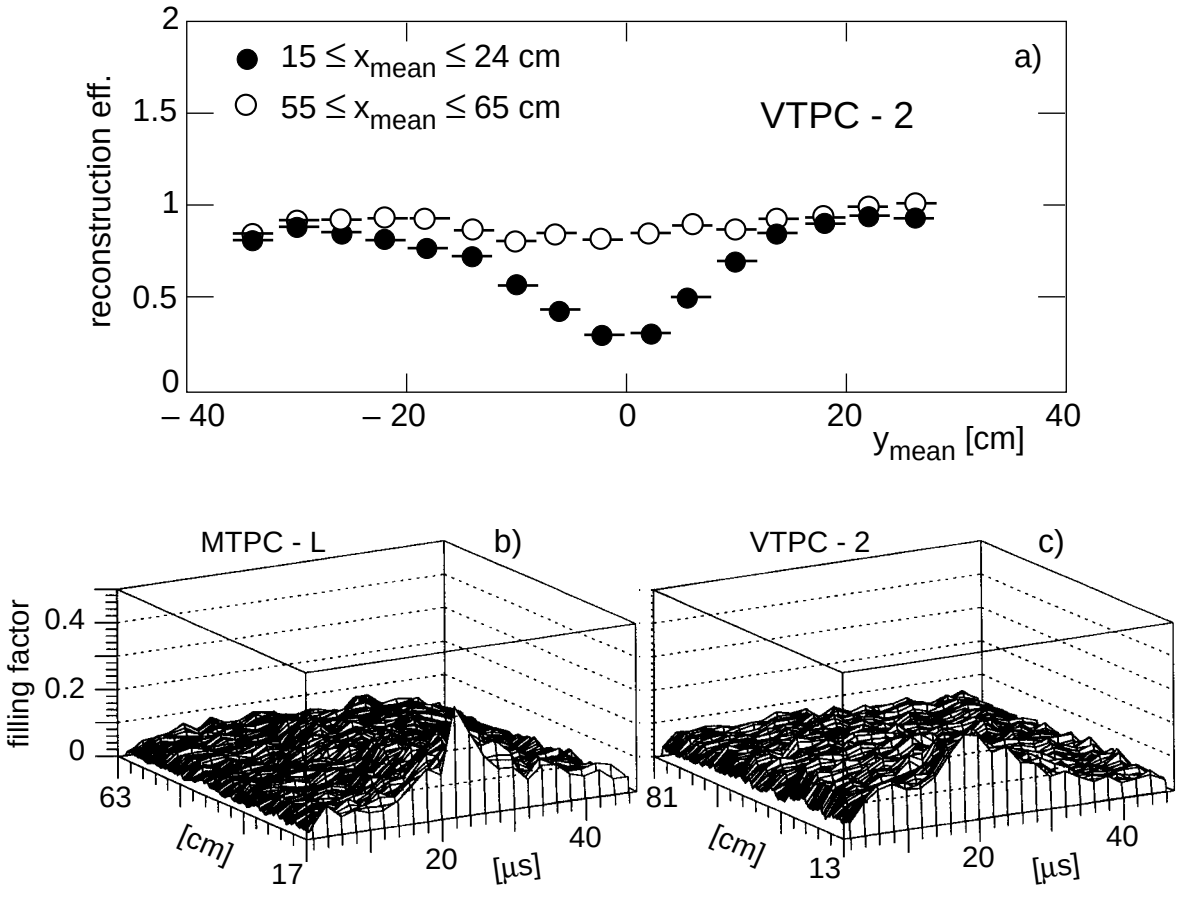

Figure 24: a) Reconstruction efficiency of tracks in two different regions far from and close to the beam as function of drift length for VTPC-2; b) and c) occupation density as function of drift time and distance from the beam for MTPC-L and VTPC-2 respectively.

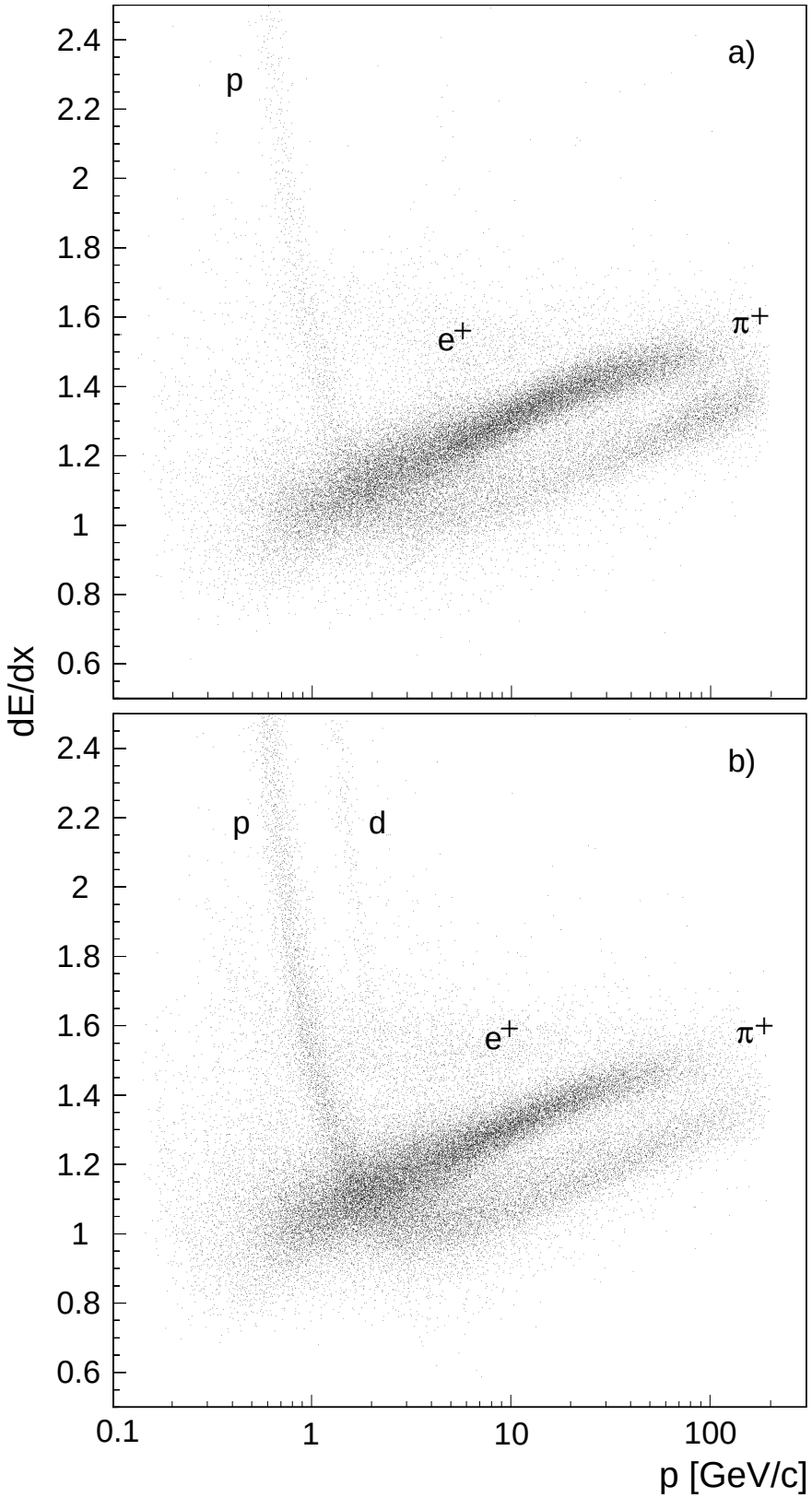

Figure 25: dE/dx as function of momentum for positive particles produced in a) p+p and b) p+Pb collisions.

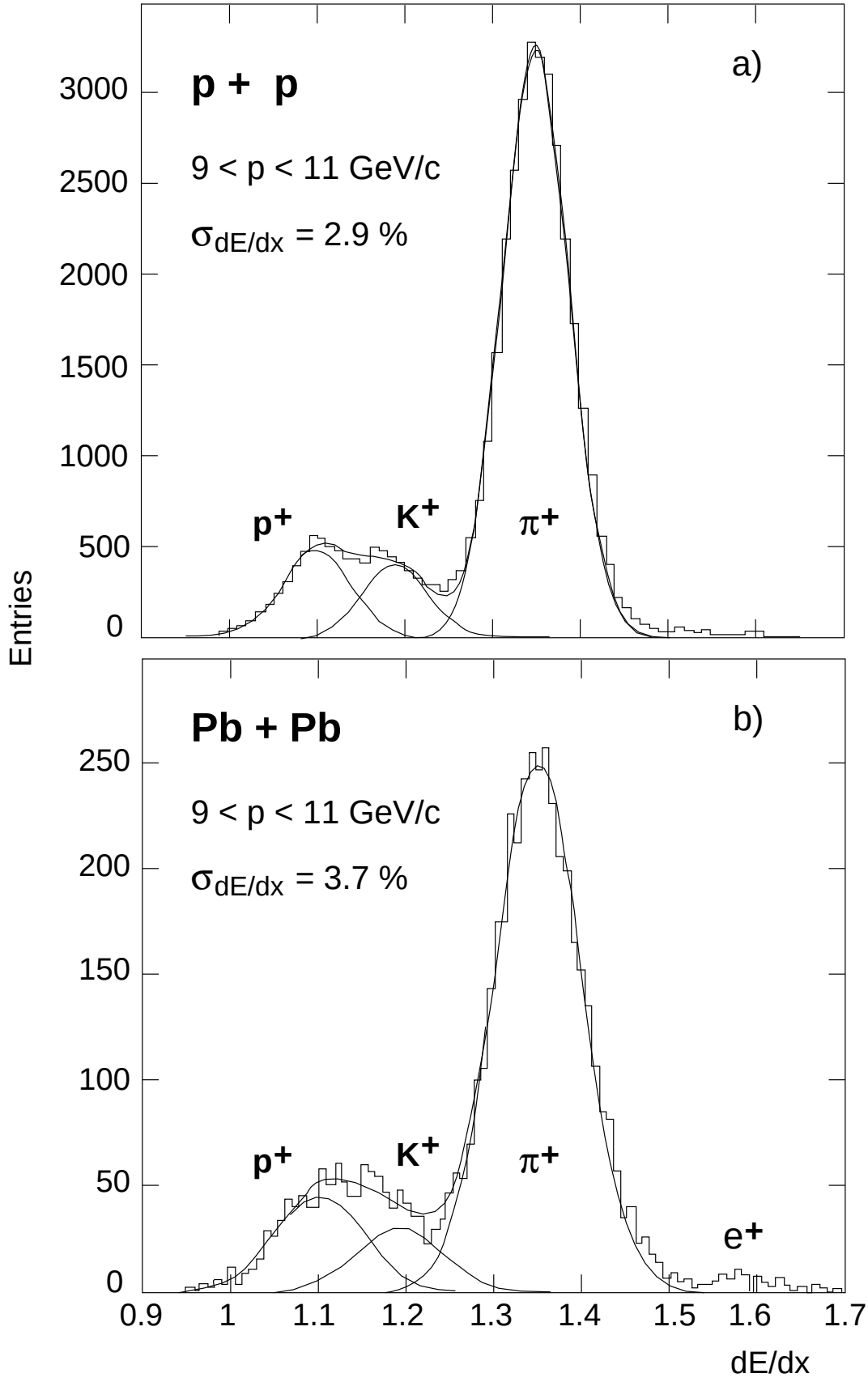

Figure 26: dE/dx distribution at a fixed momentum of 10 GeV/c for a) p+p interactions and b) central Pb+Pb collisions.

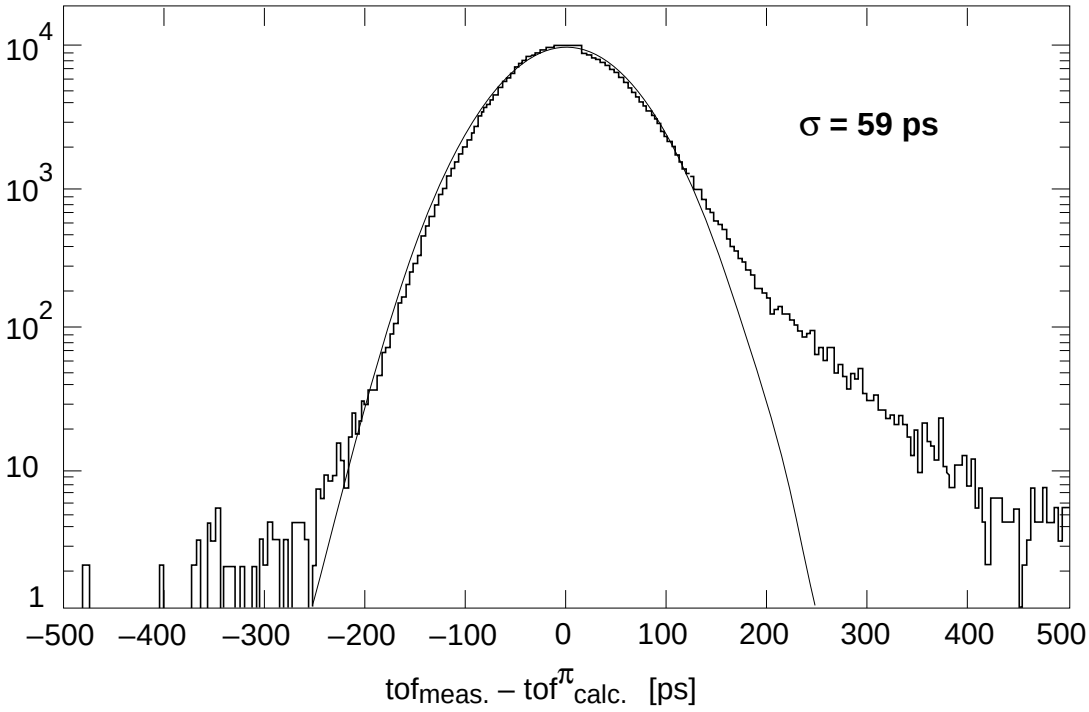

Figure 27: Time spectrum of the TOF system for central Pb+Pb events indicating the measured time resolution. The curve shows a fitted Gaussian for comparison.

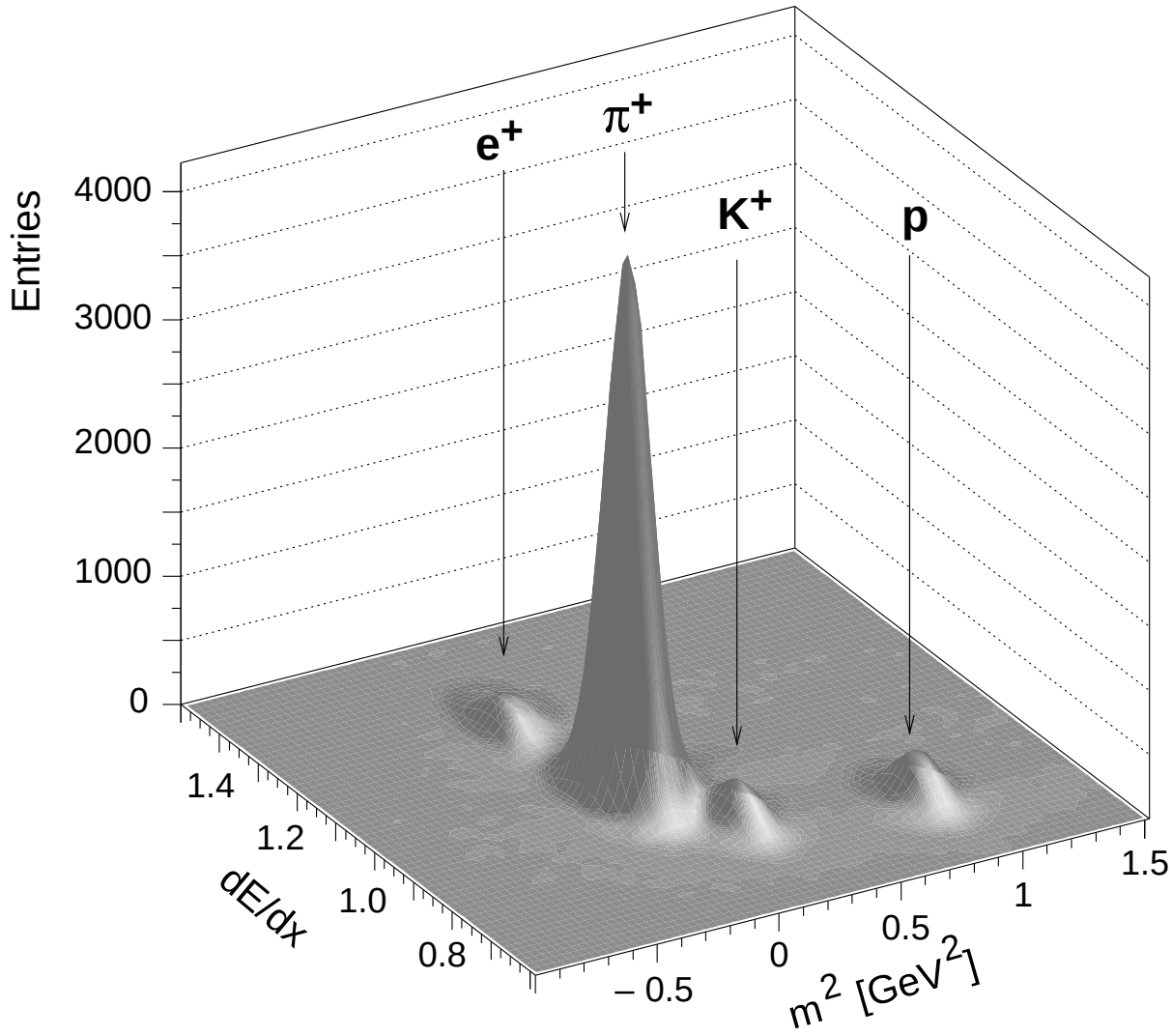

Figure 28: Particle identification by simultaneous dE/dx and TOF measurement in the momentum range 5 to 6 GeV/c for central Pb+Pb collisions.